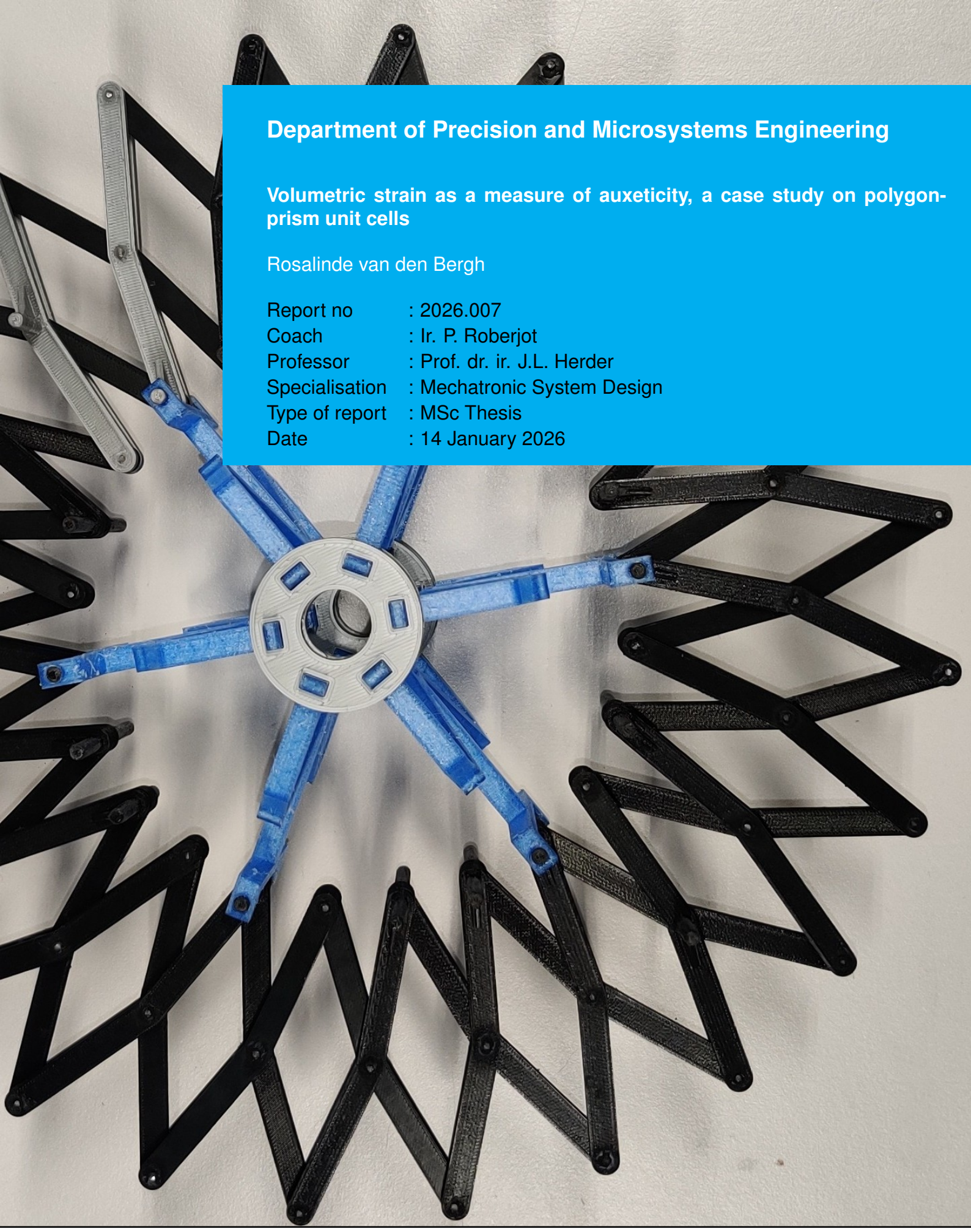

Department of Precision and Microsystems Engineering

Volumetric strain as a measure of auxeticity, a case study on polygon-prism unit cells

Rosalinde van den Bergh

Report no	: 2026.007
Coach	: Ir. P. Roberjot
Professor	: Prof. dr. ir. J.L. Herder
Specialisation	: Mechatronic System Design
Type of report	: MSc Thesis
Date	: 14 January 2026

TU Delft Delft University of Technology

Challenge the future

Preface

Throughout my mechanical engineering studies, I have always enjoyed seeing projects come to life and discovering whether reality matched our ideas. That is exactly what I set out to do during my thesis as well: to design something and actually bring it into existence.

The main difference compared to those first-year projects was that, for the very first time, I had to work on my own. To balance this, I joined Sustainable Student Consultancy, which allowed me to have social interaction and teamwork alongside my thesis work. This turned out to be a valuable addition, as I was surrounded by inspiring students and companies during my working hours. In hindsight, however, the fear of working alone was unnecessary. Pierre and Just were closely involved throughout the entire project, and for that I am deeply grateful. I would like to thank them for their enthusiasm, their guidance, and for always thinking along with me. Most importantly, I appreciate how they consistently reminded me that while a project like this could always be extended further, it is also important to recognise when it is good enough, and that my health should always take priority over academic work.

Unfortunately, this thesis period was also marked by an unexpected physical setback. In April, I tore my ACL, which forced me to significantly adjust my planning. For at least six weeks, I was unable to walk and therefore unable to manufacture and test my design. Fortunately, I was able to carry out this experimental work during the summer, shortly before undergoing surgery, which then prevented me from visiting the university for another three months. During this challenging period, my thesis became something that helped keep me occupied and, at times, distracted me from the pain. Once again, I would like to thank my supervisors for their understanding and support during this time. Above all, I am deeply grateful to the people close to me, who supported me when I was highly dependent on them.

Everything that has happened over the past one and a half years has shaped this thesis. I am glad that it has now come to an end, and I look back on the process with both pride and a smile.

This document consists of two parts: my literature study and my thesis.

Delft University of Technology

ME-HTE Literature Research
(ME56010)

Classification and design of 3D auxetic metamaterials based on topology

Author:
Rosalinde van den Bergh (4840011)

Supervisors:
Just Herder
Pierre Roberjot

March 20, 2025

Abstract

Auxetic metamaterials are engineered structures that exhibit a negative Poisson's ratio, resulting in transversal expansion when subjected to a lateral stretch. This volumetric deformation has numerous potential applications in fields such as robotics, healthcare, and structural engineering. With advancements in manufacturing techniques in recent years, research into these materials has grown significantly.

However, there is currently no systematic overview of the existing research, leading to repeated examination of the same structures without fully exploring the potential range of mechanical properties.

This literature review proposes an analysis of the existing 3D auxetic metamaterials and a categorization for 3D auxetic metamaterials. The unit cells are categorized based on their base topology, modifications to this topology, and spatial configuration. This includes the order of symmetry and whether the unit cell is inherently 3D or a 2D cell projected onto a curved plane or utilizing a coupling mechanism. This categorization highlights current research trends, particularly the prevalence of cubic structures derived from 'Honeycomb' or 'Connected stars' bases. Finally, this overview serves as a foundation for inspiring new structures, with examples provided in the paper.

1 Introduction

Metamaterials are artificially engineered materials designed to exhibit properties not typically found in nature. By designing the internal geometry rather than modifying the material composition, researchers can tailor unique properties, including mechanical [1], acoustic [2], thermal [3], and electromagnetic [4] characteristics.

One particularly intriguing classification of metamaterials is characterized by their Poisson's ratio, which describes the relationship between axial and lateral strain. According to the theory of linear elasticity, isotropic materials have Poisson's ratios in the range from -1 to 0.5. However, metamaterials are not bound by these constraints and can be categorized into three groups: meotic (positive Poisson's ratio above 0.5) [5], anepirretic (zero Poisson's ratio) [6], and auxetic (negative Poisson's ratio) [7]. Auxetic materials exhibit an unusual mechanical response, expanding laterally when stretched rather than contracting, as conventional materials do.

Some structures exhibit full or 'perfect' auxeticity [8], meaning they expand in all lateral directions when stretched in one direction, while others display partial auxeticity, where this effect occurs only in certain directions. The kinematics of 3D metamaterials are typically defined by input-output relations along three independent axes, resulting in three possible strain relationships, two of which are independent. A structure is considered auxetic when at least one of these independent relationships results in a negative Poisson's ratio. A partially auxetic structure has one negative strain relation [9], while a fully auxetic structure has two [10].

In recent years, auxetic metamaterials have gained significant attention due to their novel mechanical properties and potential applications. They have been explored for impact absorption [11], energy dissipation [12], tunable stiffness [13], and enhanced fracture resistance [14], making them highly relevant for industries such as aerospace [15], the medical field [16], and protective equipment [17].

However, while extensive research has been conducted, there is no clear systematic categorization of 3D auxetic metamaterials. This lack of structure makes it difficult to assess the full scope of existing research and identify areas that remain underexplored. As a result, studies tend to focus on a limited number of well-known structures [18], leaving many other possible configurations overlooked.

To address this gap, this study introduces a systematic classification of the current literature on 3D auxetic metamaterials. By categorizing existing 3D auxetic structures, the study aims to provide an overview of the field, identify research trends, and inspire the exploration of new and innovative topologies. Firstly, we focus our classification on structural topology. Secondly, we distinguish between topology and embodiment. Embodiment refers to how the topology is shaped, and the same topology can be embodied in various ways, such as through a single-material or multi-material configuration. This distinction will be further discussed in Section 2.2.3. Additionally, we propose structural modifications that can be applied to the topology. Lastly, we propose using this classification to inspire future designs, as illustrated through the development of two novel 3D auxetic unit cells.

2 Methodology

In this section we introduce the literature search based on peer reviewed articles and the classification criteria using base topologies, spacial configuration and modifications.

2.1 Literature search

To ensure a systematic and comprehensive review of the literature, a structured approach was used to identify relevant papers on the topic of 3D auxetic metamaterials. The literature search was conducted using the Scopus

database, chosen for its comprehensive collection of peer-reviewed scientific articles and its ability to refine searches based on keywords in specific fields such as titles, abstracts, and author-defined keywords. The search was limited to articles published in English, while no restrictions were applied to the publication date, as the earliest relevant article was published in 2012.

To focus the search on the topic of interest, specific search terms were used, as described in Table 1. The search terms were categorized into three main groups: keywords related to mechanical metamaterials, auxetic structures, and the concept of three-dimensionality. It is important to note that 'three-dimensional' yields the same search results as 'three dimensional'. These terms were combined using the AND operator, ensuring that the retrieved articles addressed all three aspects of the topic.

Search field	**Search terms**
Keyword	"mechanical metamaterials" **OR** metamaterial
Keyword	auxetic **OR** auxeticity **OR** "auxetic structure" **OR** "negative poisson's ratio"
Title, abstract and keyword	"three dimensional" **OR** 3d

Table 1: Search queries in Scopus combined using an AND operator.

The search, conducted on November 25, 2024, yielded an initial set of 165 articles.

The inclusion of the term 'three dimensional' and its variations in the search query often retrieved papers in which the fabrication method—3D printing—was mentioned in the abstract or keywords, even when the structures themselves were 2D. Redefining the search terms to exclude '3D printing' was deemed unsuitable to filter out these unintentional 2D structures, as it would also remove articles on actual 3D auxetic structures.

To refine the dataset, a manual screening process was implemented. After filtering out the 2D structures, the papers were further narrowed down. Selecting papers that focus on topology design, while papers centered around mathematical models, material characterization, or medical applications were excluded, as they fell outside the scope of this review. Additionally, articles that were not accessible through institutional subscriptions were excluded from the final dataset. Following this rigorous screening process, the dataset was refined to 64 papers.

2.2 Classifications

In this section, we introduce a systematic framework to categorize these unit cells based on their base topology, spatial configuration, and modifications. The following sections elaborate on each class in detail.

2.2.1 Base topology

The base topology for the metamaterial unit cells is derived from the work of Roberjot and Herder [19]. Their study introduces a design method based on a planar three-beam minimal unit (Figure 1a), which serves as a foundation for systematically generating various structures. This approach results in six distinct categories, each representing a unique base topology explored in this study: 'Connected stars' (Cs), 'Puzzle tiles' (Pt), 'Rotating triangles' (Rt), 'Honeycomb' (Hc), 'Missing rib' (Mr), and 'Closed geometry' (Cg). These topologies are illustrated in Figure 1.

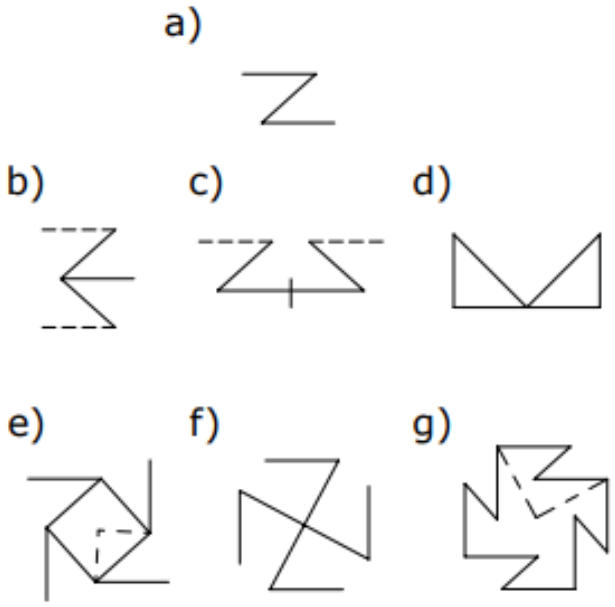

Figure 1: Representation of the planar base auxetic families from [19]: (a) Minimal base, (b) 'Connected stars', (c) 'Puzzle tiles', (d) 'Rotating triangles', (e) 'Honeycomb', (f) 'Missing rib', (g) 'Closed geometry'.

An example of the 'Connected stars' topology from the selected literature is shown in Figure 2a, where this topology is used to construct a 3D unit cell and metamaterial [20]. Lan [21] utilizes a variation of the 'Puzzle tile' topology, specifically a specialized case known as the arrowhead configuration, which involves a slight rotation of the symmetry axis. A notable example of the 'Honeycomb' structure includes a configuration where the length of the outer beams is reduced to zero, effectively transforming them into hinge points rather than structural beams, as shown in Han's study [22] (Figure 2c). Li [23] employs the 'Missing rib' topology to construct a unit cell (Figure 2d). However, the selection mentioned in Section 2.1 contains no examples of the 'Rotating triangle' and 'Closed geometry' topologies.

While most structures can be classified into one of the six base topologies, some configurations deviate from these standard categories. These outliers are categorized under the class 'Other' topology. The inclusion of this class allows us to assess whether the six primary topologies sufficiently cover the majority of structures in the selected literature. Examples of this class include origami-inspired structures [24] and bio-inspired designs [25], as they cannot be described by copy rotating any of the base topologies. Another example of an 'Other' topology is the sliding structure studied by Pan [26]. This design incorporates a non-monolithic structure where elements move relative to each other, as shown in Figure 2e. It uses a spring mechanism to maintain its 'open' position. When loaded from the top, the gray component remains stationary while the blue elements slide within it due to their relative geometry, leading to a contraction in both the x- and y-directions.

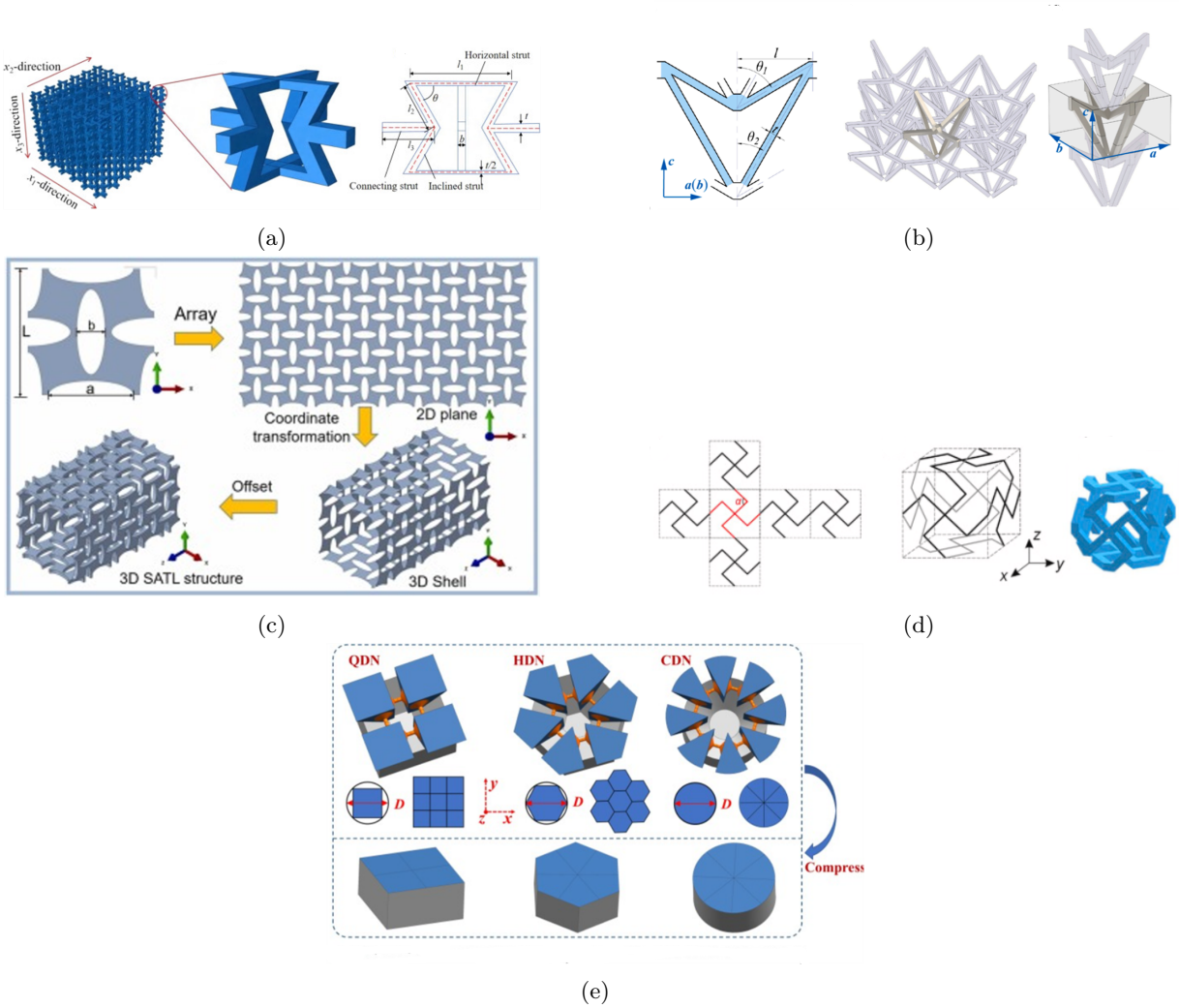

Figure 2: Examples of base topologies from the selected literature (a) Connected stars [20], (b) Puzzle tile [21], (c) Honeycomb [22], (d) Missing rib [23], and (e) 'Other' base [26].

2.2.2 Spatial configuration

The fundamental structures discussed in the previous section are 2D, serving as a basis rather than a complete unit cells. To generate 3D unit cells, these base structures must be replicated along one or more symmetry axes, which can exist within or beyond the original topology, resulting in diverse structural configurations.

To categorize these structures effectively, we identify two primary classification criteria:

1. The way in which the auxetic unit cell occupies 3D space
2. The symmetry characteristics of the unit cell

These criteria have been chosen because they highlight significant differences in mechanical behavior and with that, potential applications. It captures the topology differences rather than the embodiment. Moreover, almost all of the structures from the selected literature can be captured in this distinction.

Volume expansion

One of the key aspects that distinguishes different 3D auxetic unit cells is how they fill a 3D volume. This can occur in three distinct ways:

- 2D auxetic cells with a coupling mechanism to the third dimension:

Some structures extend an initially 2D auxetic unit cell into the third dimension by incorporating a coupling mechanism. This approach preserves the auxetic properties of the original 2D pattern while enabling deformation

in 3D space. For instance, as illustrated in Figure 3a, a 'Connected stars' base with curved beams is linked to the next layer through crossing beams. This coupling mechanism establishes a negative correlation between strain in the z-direction and the x- and y-directions. However, the coupling itself does not necessarily need to be auxetic; in many cases, it results in a partially auxetic structure, where only certain deformation modes exhibit auxetic behavior.

- 2D unit cells mapped onto a curved surface:

In this category, auxetic structures conform to a curved plane rather than occupying a traditional 3D volume. These structures maintain their auxetic behavior while adapting to non-planar geometries. Unlike the previous category, they do not require a coupling mechanism, as the curvature of the plane itself causes the overall structure to extend into 3D space while the unit cell remains fundamentally 2D. An example of this can be seen in Figure 2c or Figure 3b, where a 'Honeycomb'-based structure forms a tubular shell while preserving the auxetic properties of the original 2D unit cell.

- Intrinsic 3D auxetic unit cells:

Unlike the previous two approaches, these truly 3D structures exhibit a volumetric auxetic response, meaning that the auxetic effect is inherently 3D rather than derived from a 2D configuration. Teng [18] demonstrates this by presenting multiple configurations for transforming a 'Connected stars' base into a volumetric unit cell, as shown in Figure 3c.

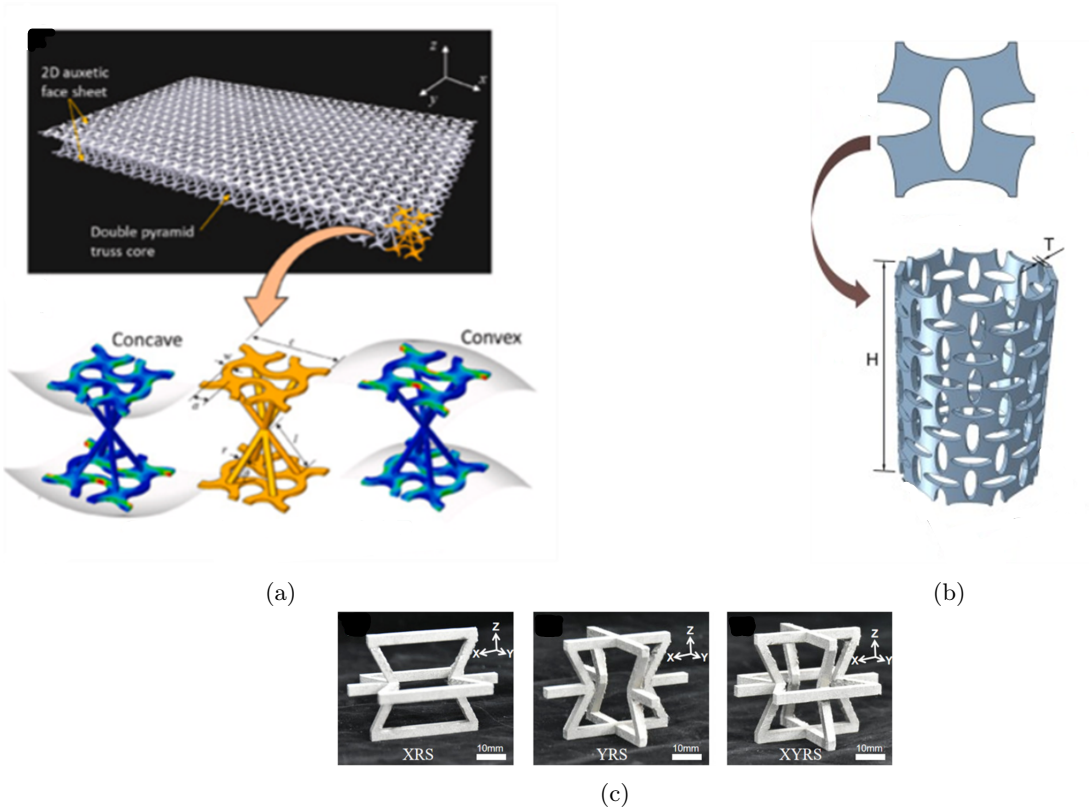

(a) (b)

(c)

Figure 3: Examples of space-filling possibilities from the selected literature: (a) a 2D unit cell with a coupling mechanism [27], (b) a 2D unit cell on a curved plane [28], and (c) an inherent 3D unit cell [18].

Order of symmetry Another critical aspect for the classification of 3D auxetic unit cells is their symmetry. The order of symmetry of a structure influences its mechanical response, determining properties such as directional stiffness, deformation behavior, and energy absorption, which in turn affect its suitability for specific applications. This classification is based on the n-fold symmetry of the unit cell, which defines the number of symmetry axes or planes within the structure. The number of symmetry axes can lead to fundamentally different auxetic behaviors, whereas the shape of the unit cell primarily serves as a design choice and does not inherently determine its mechanical properties.

Low-symmetry structures have fewer symmetry elements, such as those based on orthogonal axes, and typically exhibit directionally dependent mechanical properties. High-symmetry structures include unit cells

with hexagonal, or other highly symmetric configurations, which tend to exhibit more uniform mechanical behavior in multiple directions. The number of symmetry folds defines distinct topological configurations, while the specific geometric realization—such as whether the structure adopts the shape of a cube or a hexagonal prism—is a matter of design embodiment. Examples of different symmetrical structures are provided below to illustrate their variations and implications.

The study by Teng [18], as shown in Figure 3c, presents a four-fold structure in a cubic configuration. In contrast, Figure 4 depicts a unit cell designed by Peng and Bargmann [29], featuring a 6-fold structure derived from the same 'Connected stars' base. Despite both unit cells sharing the same base topology and embodying a cuboid shape, they exhibit inherently different structural characteristics. This highlights the significance of symmetry as a classification criterion, demonstrating that variations in the order of symmetry can lead to fundamentally distinct auxetic behavior.

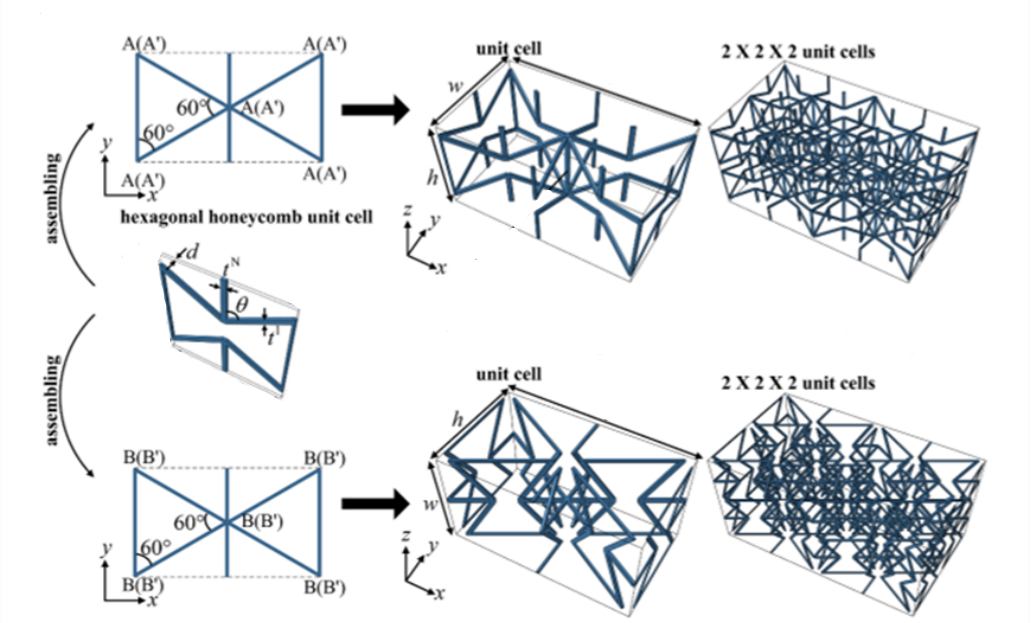

Figure 4: A 6-fold unit cell with a cuboid embodiment from [29], demonstrating that the order of symmetry does not necessarily correspond to the shape of the unit cell.

2.2.3 Modifications

The third classification, 'modification', is defined in our work as a change in the base structure that results in a significant alteration of its mechanical response relative to the original configuration. Although these modified structures are still based on the fundamental topologies introduced in Section 2.2.1 and generally retain similar mechanical properties, they exhibit notable differences that set them apart from their unmodified forms. Here, 'mechanical response' includes not only Poisson's ratio but also other structural properties—such as load-bearing capacity, stiffness along multiple axes, and thermal behavior—that are critical for most practical applications.

For example, a mechanism that preserves the original topology while not being monolithic—such as the design presented in [30] Figure 5a—is not considered a modification. Instead, it is classified as an embodiment variation resulting from manufacturing choices. In contrast, Figure 5b depicts a true topological modification, where the introduction of curved beams fundamentally alters the structure's mechanical response, including its stiffness characteristics. This design is characterized as a four-fold planar structure with a coupling mechanism to the third dimension. Specifically, the blue curved beams function as the "arms of the 'Honeycomb'," with the coupling mechanism integrated into the "belly of the 'Honeycomb' ". Furthermore, the light blue cross and purple curved beams replace the conventional flat square, thereby enabling coupling into the third dimension.

It is important to note that the presence of curved beams does not necessarily indicate a topological modification. In the study by Zhang [31], a four-fold 'Honeycomb' structure is examined, featuring a central ring (Figure 5c). While Zhang refers to this region as a ring, its circular shape inherently implies the presence of curved beams instead of the straight beams that would otherwise form a cubic geometry. However, this central region is designed to rotate rather than deform, meaning that its specific shape does not significantly affect the mechanical behavior. As a result, this design is classified as an embodiment variation rather than a true topological modification.

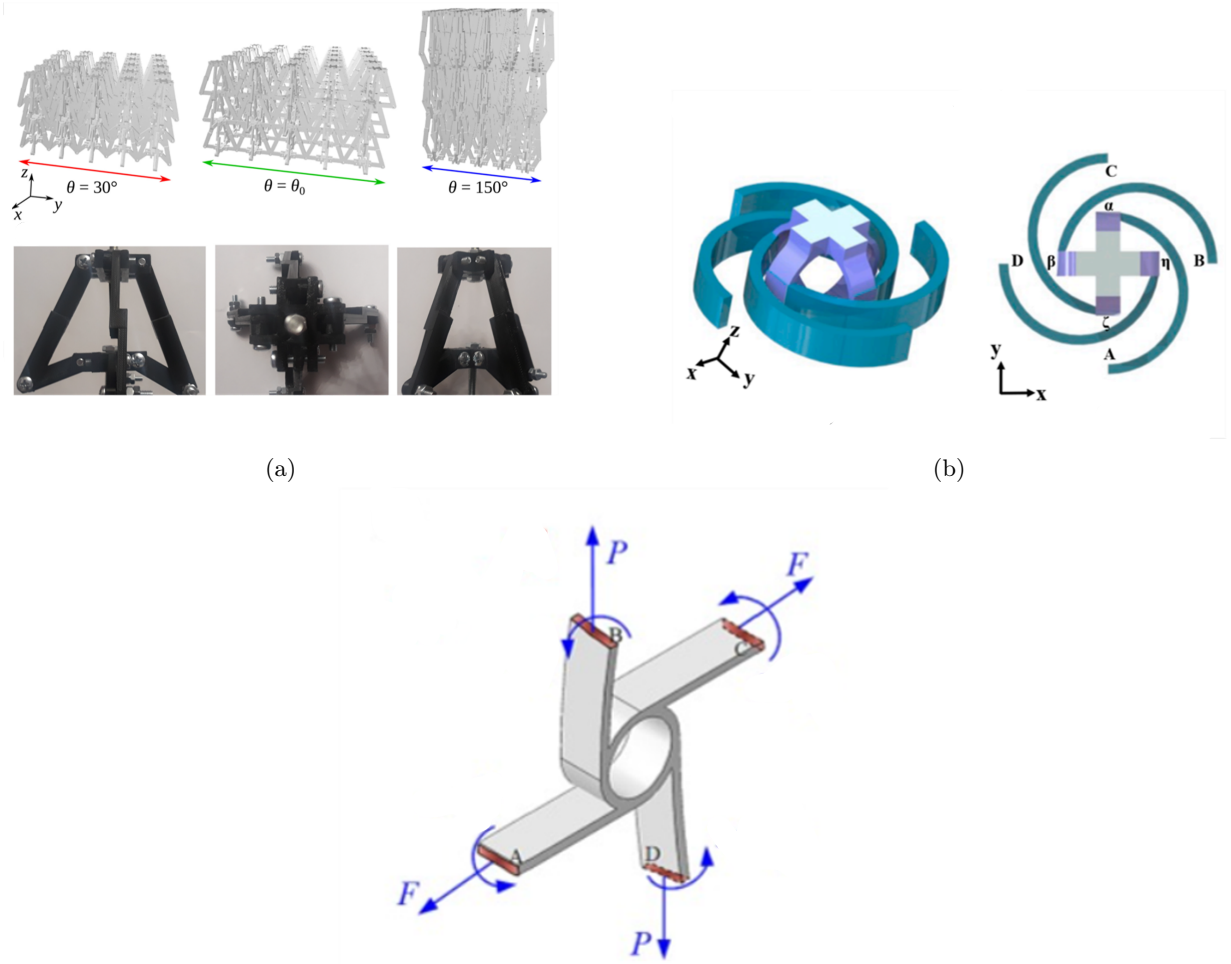

(a) (b)

(c)

Figure 5: Examples of the differentiation between embodiment and modification: (a) Non-monolithic structure, where the embodiment choice does not significantly affect the mechanical response [30]. (b) Modified unit cell, where the mechanical response is altered due to the curved beams [32]. (c) Structure with curved beams that does not qualify as modified, as the curved beams do not deform [31].

The literature presents several modifications to base structures; the three most relevant modifications will be highlighted in this section.

- Curved beams

The first modification discussed is the use of curved beams, previously shown. This modification can be beneficial for multiple reasons, such as achieving desired stiffness curves or establishing specific kinematic relationships. Curved beams also help mitigate stress concentrations by eliminating sharp corners, leading to more uniform stress distribution.

- Hierarchical structure

Another useful modification is the implementation of a hierarchical structure. In such a design, an element of the unit cell—such as a beam or a square—functions as a mechanism itself. This internal mechanism can be auxetic, enhancing the negative Poisson's ratio, or it can serve a different mechanical function. By incorporating hierarchical structuring, designers can embed specific functionalities within the auxetic design to tailor its mechanical response. In our classification, if a unit cell exhibits multiple hierarchical mechanisms, it is categorized according to the mechanism with the highest order.

For example, Dudek [33] utilizes a combination of rotating auxetic and non-auxetic structures to achieve the desired deformation pattern, as illustrated in Figure 6a.

- Meotic structure

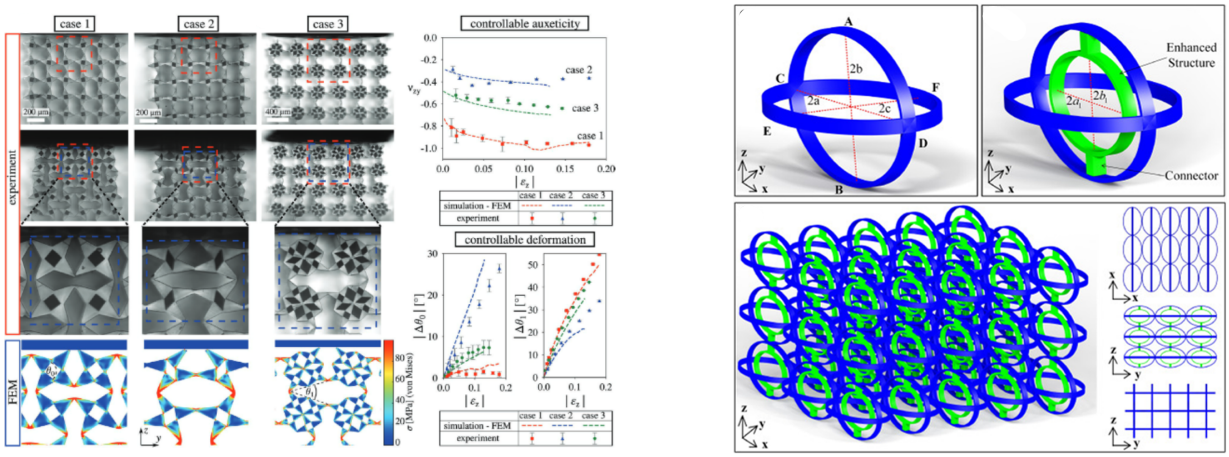

(a) (b)

Figure 6: Examples of modifications from the selected literature (a) A hierarchical structure to achieve controllable deformation [33] (b) A meotic structure [34].

Finally, another modification observed in the selected literature is the use of a structure with a positive Poisson's ratio, known as a meotic structure. In this approach, the angles of the auxetic base are adjusted to yield a positive Poisson's ratio in specific directions. For instance, in the unit cell presented by Wang [34] (Figure 6b), this configuration is applied to define the relationship between the x- and y-directions, as well as between the x- and z-directions. As a result, these two positive correlations induce a negative relationship between the z- and y-directions, forming one of the input–output relationships and making the structure partially auxetic, as defined in the introduction. Wang's design is based on a 'Connected star' topology and incorporates curved beams.

3 Results

The table below organizes the literature selected for this study based on the classifications proposed in Section 2.2. The unit cells described in each study are assigned to their corresponding categories. Some references appear in multiple categories, as these studies explore multiple unit cell designs. Furthermore, not all proposed designs have undergone experimental validation. The structures in the table, which serve primarily as conceptual suggestions rather than fully developed designs, are written in bold.

The proposed classification is considered comprehensive along both dimensions. The base topology categories are derived from the families outlined in Roberjot's paper [19] and are supplemented by an 'others' category, as well as a modified version for each base topology. Eighty percent of the structures found in the selected literature can be described by the defined base topologies and their modifications, demonstrating that Roberjot's classification is sufficient for the purpose of this study. This allows us to draw relevant conclusions about the research trends. The y-axis represents the space-filling possibilities, with 'volume' corresponding to the highest order for three-dimensional structures. By definition, a one-dimensional structure—such as a line—exhibits movement in only one direction; therefore, it does not couple movements along multiple axes and cannot be characterized by a Poisson's ratio. This inherently excludes the possibility of a one-dimensional auxetic material. Although a curved line could theoretically be used to form a plane, which—when combined with a coupling mechanism—might serve as the basis for a three-dimensional metamaterial, such configurations have not been observed in the literature and currently do not offer any practical advantages; consequently, they are not included in this overview.

Base Structures	**Plane**			**Curved Plane**			**Volume**			**Total**
	2F Plane	4F Plane	Other Plane	2F Curved Plane	4F Curved Plane	Other Closed Plane	4F Volume	6F Volume	Other Volume	
Connected stars, CS				[35],[36],[37]			[38],[39],**[40]**, [41],**[42]**,[43], **[44]**,[20],[45], [46],[18],[47], [48]	[38],**[29]**		18
Connected stars (modified)	[27],[49],[50]			[51],[52]			[53],[54],**[55]**, [34],[56],[57]	**[58]**		12
Puzzle tiles, PT							[59],[30],[21]		[60] (inf.F)	4
Puzzle tiles (modified)							[61]	**[61]**	**[61](3F), [61](8F), [61](10F)**	5
Rotating triangles, RT										0
Rotating triangles (modified)										0
Honeycomb, HC		[62],[63],[18]	[64](6F)		[22],[28],[65], [66],[31]		[67],[68],[52]	**[67]**		13
Honeycomb (modified)		[32]			[28]		[33],[69],[70], **[55]**,[71],[72]			8
Missing rib, MR							[23],**[73]**			2
Missing rib (modified)							[74]			1
Closed geometry, CG										0
Closed geometry (modified)										0
Other		[26], **[75]**	**[26](6F), [26](10F), [75] (3F)**		**[76]**	**[76](6F)**	[77],[24],[78], **[76]**,[79],[80]	[46]	**[76](3F)**, [25](2F)	16
Total	3	6	4	5	7	1	41	6	6	79

Table 2: This table presents the unit cells from the reviewed literature, categorized according to their spatial configuration and base topology. Some references describe multiple unit cells, which are included in all corresponding cells of the table. Structures that have not been experimentally validated are highlighted in bold. The notation (#F) represents the order of symmetry, indicating the n-fold structure. The green and purple cells indicate regions where structures will be introduced later in this section.

This table aims to serve two primary purposes. First, it provides insight into which structures are most frequently explored in the selected literature. Second, the table serves as a tool for inspiring new structures by exploring possible combinations of existing unit cells. This process is illustrated below.

For example, the row corresponding to the 'Puzzle tile' topology contains several entries, but remains relatively sparse. Specifically, while there are three examples of 4-fold volumetric structures, such as in the study of Lan [21], the 6-fold volumetric category remains empty, as highlighted in green in Table 2. To generate a 6-fold 'Puzzle tile' structure, one approach is to combine an existing 4-fold 'Puzzle tile' reference with a 6-fold structure from another base topology. A relevant example of this can be found in the work of Bückmann [38], where both 4-fold and 6-fold 'Connected stars' structures are demonstrated. Using a similar methodology, a new 6-fold 'Puzzle tile' structure has been developed and is presented in Figure 7.

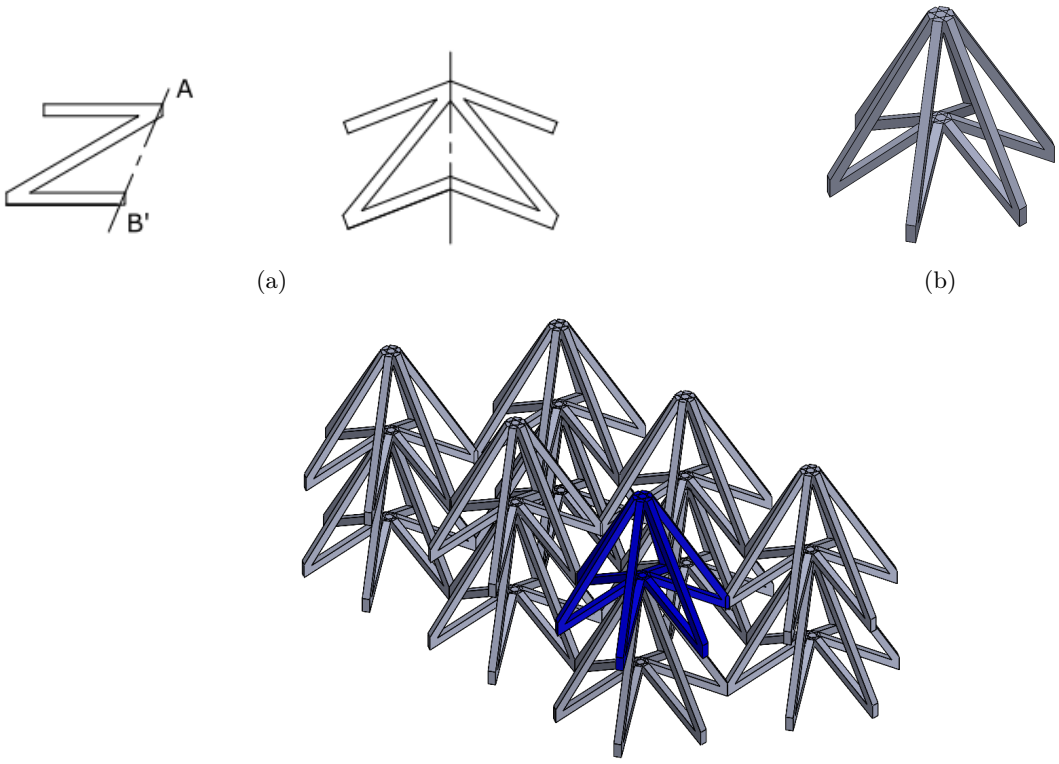

(a) (b)

(c)

Figure 7: A six-fold 'Puzzle tile' structure that can be created by combining references to fill the green cell in Table 2, formed by combining [21] and [38]: (a)'Puzzle tile' to arrowhead from Roberjot [19], (b) 6-fold 'Puzzle tile' unit cell, (c) tessellation of the 6-fold 'Puzzle tile'.

A missing entry in the table can be filled by identifying compatible references within the same row and column and exploring their combination. Additionally, modifications applied to one base topology can often be extended to others, further expanding the design space.

Even when a cell lacks a directly compatible reference in the same row or column—or in both—it remains possible to propose a solution, although additional input from the designer may be required. For instance, the 'Closed geometry' category has no examples in this literature set. In this paper, the 3-fold 'Closed geometry' from Roberjot [19] is combined with the 'Missing rib' structure from Li [23] (see Figure 2d). In this case, the conventional 4-fold cubic structure is effectively translated into a 3-fold structure, namely the tetrahedron. The resulting structure can be seen in Figure 8.

Overall, there is no evidence to suggest that any cell in the table is inherently impossible to fill. The examples provided illustrate how missing entries can be addressed, whether through the use of compatible references or through creative design. In this way, the classification not only reflects current research trends but also serves as an inspiration for future innovations.

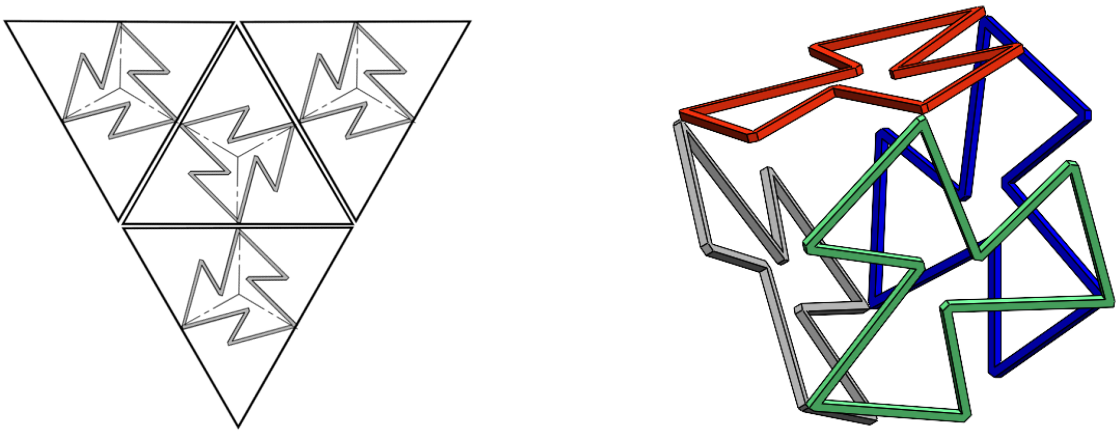

(a) (b)

Figure 8: A newly created 'Closed geometry' 3-fold structure to fill the purple cell in Table 2: (a) Flattened representation of the structure, (b) isometric view of the unit cell.

4 Discussion

4.1 Current research trends

Table 2 clearly indicates that research efforts have not been evenly distributed across all configurations.

First, regarding the base topologies; the 'Connected stars' and its modifications account for 30 out of the 79 unit cells, and the 'Honeycomb' contributes another 21. Together, these two categories represent nearly 80% of the 63 unit cells derived from the base topologies identified by Roberjot [19], highlighting their dominance in the literature. The 'Puzzle tile' and 'Missing rib' topologies are also represented, although they are less common. However, the 'Rotating Triangles' and 'Closed geometry' topologies are entirely absent from this selection.

The 'Other' category, which includes structures that do not fit neatly into one of the defined base topologies, is largely composed of designs that lack experimental validation. The only exception is the 4-fold volumetric category, where most structures have undergone experimental validation. Moreover, this category appears to suggest that one-fifth of the structures cannot be classified under the established base topologies. However, this presents a somewhat distorted perspective. For example, the study by Ma [76] contributes four structures within this category, none of which have been experimentally validated. Some of these structures in this category could still be traced back to an existing base topology, but their classification is not immediately apparent.

Examining the table by columns; the volumetric unit cells constitute the largest category, comprising 53 of the 79 structures. Additionally, within each classification, 4-fold symmetric structures consistently have the highest representation. More than half of all unit cells fall under the 4-fold volumetric category, indicating a strong preference for cubic unit cells. This preference is especially evident in unit cells based on the (modified) 'Connected stars' topology, which is the most frequently encountered configuration for 3D mechanical metamaterial unit cells.

Non-cubic volumetric unit cells, on the other hand, are rarely experimentally validated. For instance, Rogers' study [61] presents multiple designs for non-cubic volumetric unit cells. However, the authors ultimately select a cubic unit cell for testing, stating: "The cubic unit cell was selected because the tessellation and visual calculation of the Poisson's ratio for this cell is mathematically simple." This illustrates a potential reason for the dominance of cubic cells: experimental testing equipment is often designed to measure mechanical responses along two or three perpendicular axes, which aligns well with the symmetry of cubic structures. In contrast, structures with a higher number of symmetry folds typically exhibit dependent axes of movement, complicating mechanical testing and characterization. Another factor contributing to the prevalence of cubic unit cells is the conventional definition of Poisson's ratio, which relies on the relationship between strain in the x-, y-, and z-directions. This makes it straightforward to apply to cubic unit cells but less convenient for structures with different-order symmetries. However, an alternative approach could mitigate this issue: using compressibility instead of Poisson's ratio. Compressibility measures the overall change in volume, independent of direction, making it a more suitable parameter for comparing all 3D unit cells, regardless of their symmetry or auxetic behavior [81].

4.2 Developing new 3D auxetic metamaterials

The second primary objective of this study was to inspire the exploration of new topologies. The examples presented in the previous section demonstrate that this goal has been achieved. The current organization of the literature reveals clear research gaps, and the relevant references to address these gaps are easily accessible, thus minimizing the time and effort required to create new structures. However, within each category, significant design variation can still occur due to modifications and the choice of symmetry axes. The table proves successful in assisting the identification of a broader range of potential structures.

4.3 Limitations and future recommendations

The classification table presented in this study provides a structured overview of 3D auxetic unit cells, effectively highlighting the most extensively explored topologies and modifications, and offering valuable insights into current research trends. Additionally, it serves as an inspiration for new designs by identifying gaps in the existing literature. However, while the table is a useful tool, there are certain limitations that also present opportunities for future research.

Not all three-dimensional structures can be fully captured within this classification, as it is based on a two-dimensional base topology. For example, the structure presented by Lai [70], shown in Figure 9, bears resemblance to a honeycomb configuration. However, it cannot be generated by simply replicating a 2D honeycomb around a single point or axis. In this study, it is categorized as a 'modified' structure, but introducing a classification based on a truly three-dimensional base could provide a more precise representation of such cases. This would not only provide a more accurate representation of the existing literature, but also open up possibilities for a wider range of structures, potentially leading to a greater variety of mechanical properties. However, the development of a 3D base structure design method is still lacking, and creating one was beyond the scope of this study. The current classification method, while limited in this regard, effectively serves its purpose in identifying and categorizing the most extensively researched auxetic structures.

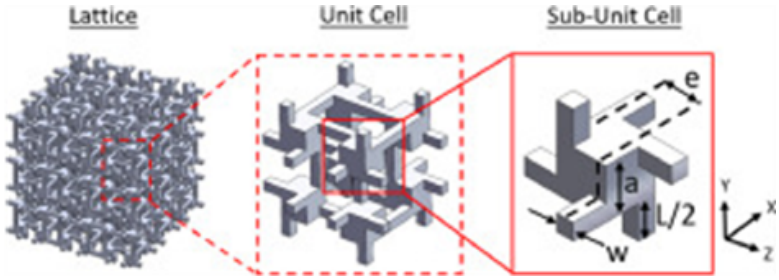

Figure 9: Modified 'Honeycomb' unit cell [70]. A three dimensional base topology would be needed to describe this structure accurately.

Section 2.2.3 highlights the most commonly used and relevant modifications that can be applied across multiple base topologies. The goal of this section is to inspire future research to incorporate these modifications into the design processes. However, these are not the only modifications observed in the literature selected for this study. For example, the out-of-plane base structure shown in Figure 9 also represents a notable variation.

The classification of 'modified' includes a broad range of structural changes, meaning that the exact geometry and mechanical behavior of a unit cell cannot be directly determined from Table 2 if the structure is modified. A possible solution could be; creating a extensive modification selection menu which would indicate the nature of the modification. However, the selection of modifications presented in this study is not exhaustive. It is based on the literature set analyzed in this work, but there may well be additional modifications that have yet to be explored.

As previously discussed, most research has focused on cubic unit cells, which have the limitation of aligning their load-bearing capacities with the principal planes of the structure. Exploring higher-order symmetry structures could be valuable, as they offer more principal planes, potentially enhancing their robustness and improving their mechanical stability. However, increasing the number of structural elements typically leads to greater material usage and, consequently, higher weight. The optimal structure ultimately depends on the specific application requirements. Nonetheless, further investigation into non-cubic structures would provide deeper insights into their mechanical performance, enabling more informed decisions when selecting the most suitable configuration for a given application.

5 Conclusion

In this paper, we have proposed a systematic categorization of the current literature on 3D auxetic metamaterials to provide insight into which topologies are most frequently explored. Our framework clarifies the prevailing base topologies and spatial configurations within the field. Furthermore, the chosen categories are designed to inspire new designs: they are specific enough to leave portions of the classification table unfilled—thus inviting the development of novel unit cells, such as the new structure we have developed as an example. Yet, this approach is broad enough to cover a complete view of current research. Overall, this categorization not only highlights current trends but also lays a solid foundation for future innovations in the design of 3D auxetic metamaterials.

References

[1] Yiqiang Wang and Ole Sigmund. "Quasiperiodic mechanical metamaterials with extreme isotropic stiffness". In: *Extreme Mechanics Letters* 34 (Jan. 2020), p. 100596. ISSN: 2352-4316. DOI: 10.1016/j.eml.2019.100596.

[2] Xiyue An et al. "3D acoustic metamaterial-based mechanical metalattice structures for low-frequency and broadband vibration attenuation". In: *International Journal of Solids and Structures* 191-192 (May 2020), pp. 293–306. ISSN: 0020-7683. DOI: 10.1016/j.ijsolstr.2020.01.020.

[3] Xiaoyue Ni et al. "2D Mechanical Metamaterials with Widely Tunable Unusual Modes of Thermal Expansion". en. In: *Advanced Materials* 31.48 (2019), p. 1905405. ISSN: 1521-4095. DOI: 10.1002/adma.201905405.

[4] Maria Sakovsky, Jan Negele, and Joseph Costantine. "Electromagnetic Reconfiguration Using Stretchable Mechanical Metamaterials". en. In: *Advanced Science* 10.6 (2023), p. 2203376. ISSN: 2198-3844. DOI: 10.1002/advs.202203376.

[5] Q. Li et al. "A comparative study on mechanical and vibroacoustic performance of sandwich cylindrical shells with positive, negative, and zero Poisson's ratio cellular cores". In: *Journal of Ocean Engineering and Science* 9.4 (2024), pp. 379–390. DOI: 10.1016/j.joes.2022.08.006.

[6] H. Zhu and H. Fan. "Manufacturing and testing of CFRC sandwich cylinder with zero-Poisson's-ratio Kevlar meta-honeycomb core layer". In: *Composites Science and Technology* 230 (2022). DOI: 10.1016/j.compscitech.2022.109774.

[7] Junhyun Kim et al. "Regularly configured structures with polygonal prisms for three-dimensional auxetic behaviour". In: *Proceedings of the Royal Society A: Mathematical, Physical and Engineering Sciences* 473.2202 (2017), pp. 2030–2033. ISSN: 1364-5021. DOI: 10.1098/rspa.2016.0926.

[8] Yuping Chang and Hong Hu. "3D Fabrics with Negative Poisson's Ratio: A Review". en. In: *Applied Composite Materials* 29.1 (Feb. 2022), pp. 95–108. ISSN: 1573-4897. DOI: 10.1007/s10443-021-09931-w.

[9] Jing Huang et al. "Partial auxetic behavior of 3D mesh fabric under compression". EN. In: *Journal of Engineered Fibers and Fabrics* 19 (Apr. 2024). Publisher: SAGE Publications Ltd STM, p. 15589250241252636. ISSN: 1558-9250. DOI: 10.1177/15589250241252636.

[10] Andrea Sorrentino et al. "Bio-inspired auxetic mechanical metamaterials evolved from rotating squares unit". In: *Mechanics of Materials* 173 (Oct. 2022), p. 104421. ISSN: 0167-6636. DOI: 10.1016/j.mechmat.2022.104421.

[11] Jianlin Zhong et al. "Mechanical behaviors of composite auxetic structures under quasi-static compression and dynamic impact". In: *European Journal of Mechanics - A/Solids* 109 (Jan. 2025), p. 105454. ISSN: 0997-7538. DOI: 10.1016/j.euromechsol.2024.105454.

[12] Ramin Hamzehei et al. "3D-printed bio-inspired zero Poisson's ratio graded metamaterials with high energy absorption performance". en. In: *Smart Materials and Structures* 31.3 (Jan. 2022). Publisher: IOP Publishing, p. 035001. ISSN: 0964-1726. DOI: 10.1088/1361-665X/ac47d6.

[13] Xian Cheng et al. "Design and mechanical characteristics of auxetic metamaterial with tunable stiffness". In: *International Journal of Mechanical Sciences* 223 (June 2022), p. 107286. ISSN: 0020-7403. DOI: 10.1016/j.ijmecsci.2022.107286.

[14] Jianjun Zhang, Guoxing Lu, and Zhong You. "Large deformation and energy absorption of additively manufactured auxetic materials and structures: A review". In: *Composites Part B: Engineering* 201 (Nov. 2020), p. 108340. ISSN: 1359-8368. DOI: 10.1016/j.compositesb.2020.108340.

[15] A. Airoldi et al. "Design of a morphing airfoil with composite chiral structure". In: *Journal of Aircraft* 49.4 (2012), pp. 1008–1019. DOI: 10.2514/1.C031486.

[16] Mohammad Sadegh Ebrahimi et al. "Revolutionary auxetic intravascular medical stents for angioplasty applications". In: *Materials & Design* 235 (Nov. 2023), p. 112393. ISSN: 0264-1275. DOI: 10.1016/j.matdes.2023.112393.

[17] Mohammad Sanami et al. "Auxetic Materials for Sports Applications". In: *Procedia Engineering*. The Engineering of Sport 10 72 (Jan. 2014), pp. 453–458. ISSN: 1877-7058. DOI: 10.1016/j.proeng.2014.06.079.

[18] X.C. Teng et al. "A simple 3D re-entrant auxetic metamaterial with enhanced energy absorption". In: *International Journal of Mechanical Sciences* 229 (2022). DOI: 10.1016/j.ijmecsci.2022.107524.

[19] Pierre Roberjot and Just L. Herder. "A unified design method for 2D auxetic metamaterials based on a minimal auxetic structure". en. In: *International Journal of Solids and Structures* 295 (June 2024), p. 112777. ISSN: 00207683. DOI: 10.1016/j.ijsolstr.2024.112777.

[20] R. Liu et al. "VAM-based equivalent-homogenization model for 3D re-entrant auxetic honeycomb structures". In: *International Journal of Mechanical Sciences* 268 (2024). DOI: 10.1016/j.ijmecsci.2024.109013.

[21] X. Lan et al. "Phenomenological methods for defining elasticity and failure of double-arrowhead metamaterials". In: *International Journal of Mechanical Sciences* 252 (2023). DOI: 10.1016/j.ijmecsci.2023.108361.

[22] D. Han et al. "Experimental and computational investigations of novel 3D printed square tubular lattice metamaterials with negative Poisson's ratio". In: *Additive Manufacturing* 55 (2022). DOI: 10.1016/j.addma.2022.102789.

[23] T. Li and Y. Li. "Mechanical behaviors of three-dimensional chiral mechanical metamaterials". In: *Composites Part B: Engineering* 270 (2024). DOI: 10.1016/j.compositesb.2023.111141.

[24] Z. Li et al. "3D Printing of Auxetic Shape-Memory Metamaterial towards Designable Buckling". In: *International Journal of Applied Mechanics* 13.1 (2021). DOI: 10.1142/S1758825121500113.

[25] C.-C. Tung et al. "Bio-inspired, helically oriented tubular structures with tunable deformability and energy absorption performance under compression". In: *Materials and Design* 222 (2022). DOI: 10.1016/j.matdes.2022.111076.

[26] Y. Pan et al. "A novel 3D polygonal double-negative mechanical metamaterial with negative stiffness and negative Poisson's ratio". In: *Composite Structures* 331 (2024). DOI: 10.1016/j.compstruct.2024.117878.

[27] Y. Chang Jeong and K. Kang. "Mechanical design of support structure for chips embedded in a convex-deformable mobile device". In: *Results in Materials* 20 (2023). DOI: 10.1016/j.rinma.2023.100468.

[28] D. Han et al. "Lightweight auxetic tubular metamaterials: Design and mechanical characteristics". In: *Composite Structures* 311 (2023). DOI: 10.1016/j.compstruct.2023.116849.

[29] X.-L. Peng and S. Bargmann. "A design method for metamaterials: 3D transversely isotropic lattice structures with tunable auxeticity". In: *Smart Materials and Structures* 31.2 (2022). DOI: 10.1088/1361-665X/ac411f.

[30] K.K. Dudek et al. "The multidirectional auxeticity and negative linear compressibility of a 3D mechanical metamaterial". In: *Materials* 13.9 (2020). DOI: 10.3390/ma13092193.

[31] C. Zhang et al. "On the effective elastic constants of anti-tetra chiral tubular structure". In: *Engineering Structures* 278 (2023). DOI: 10.1016/j.engstruct.2022.115507.

[32] J. Cui, L. Zhang, and A.K. Gain. "A novel auxetic unit cell for 3D metamaterials of designated negative Poisson's ratio". In: *International Journal of Mechanical Sciences* 260 (2023). DOI: 10.1016/j.ijmecsci.2023.108614.

[33] K.K. Dudek et al. "Micro-Scale Auxetic Hierarchical Mechanical Metamaterials for Shape Morphing". In: *Advanced Materials* 34.14 (2022). DOI: 10.1002/adma.202110115.

[34] L. Wang et al. "Directional instability-driven strain-dependent 3D auxetic metamaterials". In: *International Journal of Mechanical Sciences* 199 (2021). DOI: 10.1016/j.ijmecsci.2021.106408.

[35] H. Mirani et al. "Tailoring of interface modes in topologically protected edge states with hourglass lattice metamaterials". In: *Journal of Sound and Vibration* 562 (2023). DOI: 10.1016/j.jsv.2023.117814.

[36] Y. Nian et al. "Nature-inspired 3D printing-based double-graded aerospace negative Poisson's ratio metastructure: Design, Fabrication, Investigation, optimization". In: *Composite Structures* 348 (2024). DOI: 10.1016/j.compstruct.2024.118482.

[37] Y. Wei et al. "A novel cylindrical mechanical metamaterial: Design, fabrication, and compressive properties". In: *Structures* 63 (2024). DOI: 10.1016/j.istruc.2024.106336.

[38] T. Bückmann et al. "Tailored 3D mechanical metamaterials made by dip-in direct-laser-writing optical lithography". In: *Advanced Materials* 24.20 (2012), pp. 2710–2714. DOI: 10.1002/adma.201200584.

[39] X. Fang, H.-S. Shen, and H. Wang. "Three-point bending behaviors of sandwich beams with data-driven 3D auxetic lattice core based on deep learning". In: *Composite Structures* 354 (2025). DOI: 10.1016/j.compstruct.2024.118751.

[40] D. Faraci, L. Driemeier, and C. Comi. "Bending-Dominated Auxetic Materials for Wearable Protective Devices Against Impact". In: *Journal of Dynamic Behavior of Materials* 7.3 (2021), pp. 425–435. DOI: 10.1007/s40870-020-00284-2.

[41] B. He, Q. Huang, and Z. Shi. "A novel three-dimensional orthogonal star honeycomb structure with negative Poisson's ratio". In: *Engineering Research Express* 6.1 (2024). DOI: 10.1088/2631-8695/ad337d.

[42] C. Li, H.-S. Shen, and H. Wang. "Postbuckling behavior of sandwich plates with functionally graded auxetic 3D lattice core". In: *Composite Structures* 237 (2020). DOI: 10.1016/j.compstruct.2020.111894.

[43] C. Li, H.-S. Shen, and H. Wang. "Full-scale finite element modeling and nonlinear bending analysis of sandwich plates with functionally graded auxetic 3D lattice core". In: *Journal of Sandwich Structures and Materials* 23.7 (2021), pp. 3113–3138. DOI: 10.1177/1099636220924657.

[44] C. Li et al. "Large amplitude vibration of sandwich plates with functionally graded auxetic 3D lattice core". In: *International Journal of Mechanical Sciences* 174 (2020). DOI: 10.1016/j.ijmecsci.2020.105472.

[45] B.J. Sahariah, A. Namdeo, and P. Khanikar. "Composite-inspired multilattice metamaterial structure: An auxetic lattice design with improved strength and energy absorption". In: *Materials Today Communications* 30 (2022). DOI: 10.1016/j.mtcomm.2022.103159.

[46] Y. Su et al. "A 3D Mechanism-driven Hexagonal Metamaterial: Evaluation of Auxetic Behavior". In: *International Journal of Mechanical Sciences* 209 (2021). DOI: 10.1016/j.ijmecsci.2021.106699.

[47] W. Wu, P. Liu, and Z. Kang. "A novel mechanical metamaterial with simultaneous stretching- and compression-expanding property". In: *Materials and Design* 208 (2021). DOI: 10.1016/j.matdes.2021.109930.

[48] X.G. Zhang et al. "Bending performance of 3D re-entrant and hexagonal metamaterials". In: *Thin-Walled Structures* 188 (2023). DOI: 10.1016/j.tws.2023.110829.

[49] Y.C. Jeong and K. Kang. "Mechanical design of a convex-deformable polymer plate". In: *Materials and Design* 231 (2023). DOI: 10.1016/j.matdes.2023.112083.

[50] C. Zhang et al. "Tunable compressive properties of a novel auxetic tubular material with low stress level". In: *Thin-Walled Structures* 164 (2021). DOI: 10.1016/j.tws.2021.107882.

[51] Y. Lyu et al. "A novel mechanical metamaterial with tunable stiffness and individually adjustable poisson's ratio". In: *Materials Today Communications* 40 (2024). DOI: 10.1016/j.mtcomm.2024.110135.

[52] X. Zhang et al. "Mechanical design and analysis of bio-inspired reentrant negative Poisson's ratio metamaterials with rigid-flexible distinction". In: *International Journal of Smart and Nano Materials* 15.1 (2024), pp. 1–20. DOI: 10.1080/19475411.2023.2246928.

[53] F. Jiang, S. Yang, and C. Qi. "Quasi-static crushing response of a novel 3D re-entrant circular auxetic metamaterial". In: *Composite Structures* 300 (2022). DOI: 10.1016/j.compstruct.2022.116066.

[54] K. Kim, H. Heo, and J. Ju. "A mechanism-based architected material: A hierarchical approach to design Poisson's ratio and stiffness". In: *Mechanics of Materials* 125 (2018), pp. 14–25. DOI: 10.1016/j.mechmat.2018.07.001.

[55] N. Novak et al. "Structural Optimization of the Novel 3D Graded Axisymmetric Chiral Auxetic Structure". In: *Physica Status Solidi (B) Basic Research* 259.12 (2022). DOI: 10.1002/pssb.202200409.

[56] C. Xu et al. "Glass Sponge-inspired Auxetic Mechanical Metamaterials for Energy Absorption". In: *Journal of Bionic Engineering* 21.5 (2024), pp. 2349–2365. DOI: 10.1007/s42235-024-00576-6.

[57] Y. Yao, Y. Ni, and L.H. He. "Rutile-mimic 3D metamaterials with simultaneously negative Poisson's ratio and negative compressibility". In: *Materials and Design* 200 (2021). DOI: 10.1016/j.matdes.2020.109440.

[58] I. Ben-Yelun et al. "GAM: General Auxetic Metamaterial with Tunable 3D Auxetic Behavior Using the Same Unit Cell Boundary Connectivity". In: *Materials* 16.9 (2023). DOI: 10.3390/ma16093473.

[59] X. Chen et al. "An Unusual 3D Metamaterial with Zero Poisson's Ratio in Partial Directions". In: *Advanced Engineering Materials* 23.4 (2021). DOI: 10.1002/adem.202001491.

[60] X. Li et al. "Plate-based cylinder metamaterial with negative Poisson's ratio and outstanding mechanical performance". In: *Science China Technological Sciences* 66.3 (2023), pp. 793–806. DOI: 10.1007/s11431-022-2212-5.

[61] B.A. Rogers et al. "Optimization and experimental validation of 3D near-isotropic auxetic structures". In: *Materials and Design* 229 (2023). DOI: 10.1016/j.matdes.2023.111844.

[62] P.-S. Farrugia, R. Gatt, and J.N. Grima. "The Push Drill Mechanism as a Novel Method to Create 3D Mechanical Metamaterial Structures". In: *Physica Status Solidi - Rapid Research Letters* 14.7 (2020). DOI: 10.1002/pssr.202000125.

[63] J. Hao et al. "A novel compression-torsion coupling metamaterial with tunable Poisson's ratio". In: *Construction and Building Materials* 395 (2023). DOI: 10.1016/j.conbuildmat.2023.132276.

[64] C. Jiao and G. Yan. "Design and elastic mechanical response of a novel 3D-printed hexa-chiral helical structure with negative Poisson's ratio". In: *Materials and Design* 212 (2021). DOI: 10.1016/j.matdes.2021.110219.

[65] J.P. Lang et al. "A star-shaped tubular structure with multiple-directional auxetic effect". In: *Thin-Walled Structures* 193 (2023). DOI: 10.1016/j.tws.2023.111247.

[66] X. Ren et al. "A simple auxetic tubular structure with tuneable mechanical properties". In: *Smart Materials and Structures* 25.6 (2016). DOI: 10.1088/0964-1726/25/6/065012.

[67] S. Babaee et al. "3D soft metamaterials with negative poisson's ratio". In: *Advanced Materials* 25.36 (2013), pp. 5044–5049. DOI: 10.1002/adma.201301986.

[68] X. Ren et al. "Design and characterisation of a tuneable 3D buckling-induced auxetic metamaterial". In: *Materials and Design* 139 (2018), pp. 336–342. DOI: 10.1016/j.matdes.2017.11.025.

[69] N. Feng et al. "A novel 3D bidirectional auxetic metamaterial with lantern-shape: Elasticity aspects and potential for load-bearing structure". In: *Composite Structures* 321 (2023). DOI: 10.1016/j.compstruct.2023.117221.

[70] C.Q. Lai, K. Markandan, and Z. Lu. "Anomalous elastic response of a 3D anti - tetrachiral metamaterial". In: *International Journal of Mechanical Sciences* 192 (2021). DOI: 10.1016/j.ijmecsci.2020.106142.

[71] A. Sorrentino and D. Castagnetti. "Novel polyhedral mechanical metamaterial exhibiting negative Poisson's ratio". In: *Smart Materials and Structures* 32.3 (2023). DOI: 10.1088/1361-665X/acb3a3.

[72] L. Wang et al. "3D Auxetic Metamaterials with Elastically-Stable Continuous Phase Transition". In: *Advanced Science* 9.34 (2022). DOI: 10.1002/advs.202204721.

[73] M. Stilz et al. "A 3D extension of pantographic geometries to obtain metamaterial with semi-auxetic properties". In: *Mathematics and Mechanics of Solids* 27.4 (2022), pp. 673–686. DOI: 10.1177/10812865211033322.

[74] L. Wang and H.-T. Liu. "3D compression–torsion cubic mechanical metamaterial with double inclined rods". In: *Extreme Mechanics Letters* 37 (2020). DOI: 10.1016/j.eml.2020.100706.

[75] X.-L. Peng and S. Bargmann. "Nacre-inspired auxetic interlocking brick-and-mortar composites". In: *Composites Communications* 48 (2024). DOI: 10.1016/j.coco.2024.101892.

[76] H. Ma et al. "Energy dissipation in multistable auxetic mechanical metamaterials". In: *Composite Structures* 304 (2023). DOI: 10.1016/j.compstruct.2022.116410.

[77] T. Li and Y. Li. "3D Tiled Auxetic Metamaterial: A New Family of Mechanical Metamaterial with High Resilience and Mechanical Hysteresis". In: *Advanced Materials* 36.15 (2024). DOI: 10.1002/adma.202309604.

[78] W. Lv, L. Dong, and D. Li. "A novel metamaterial with individually adjustable and sign-switchable Poisson's ratio". In: *European Journal of Mechanics, A/Solids* 97 (2023). DOI: 10.1016/j.euromechsol.2022.104851.

[79] F.T. Páscoa et al. “Methodology for modelling and simulation of tailored 3D functionally graded auxetic metamaterials”. In: *International Journal of Advanced Manufacturing Technology* 125.9-10 (2023), pp. 4647–4661. DOI: 10.1007/s00170-023-10863-x.

[80] J. Xu et al. “The vibration energy dissipation behaviour of 3D-PAM type RVD”. In: *Engineering Structures* 300 (2024). DOI: 10.1016/j.engstruct.2023.117142.

[81] James N. Grima-Cornish, Joseph N. Grima, and Daphne Attard. “A Novel Mechanical Metamaterial Exhibiting Auxetic Behavior and Negative Compressibility”. en. In: *Materials* 13.1 (Jan. 2020). Number: 1 Publisher: Multidisciplinary Digital Publishing Institute, p. 79. ISSN: 1996-1944. DOI: 10.3390/ma13010079.

Delft University of Technology

ME-HTE Graduation Project
(ME56035)

Volumetric strain as a measure of auxeticity, a case study on polygon-prism unit cells

Author:
Rosalinde van den Bergh (4840011)

Supervisors:
Just Herder
Pierre Roberjot

January 14, 2026

Abstract

Auxetic metamaterials are engineered structures commonly characterised by their negative Poisson's ratio, which indicates transverse expansion when the structure is stretched axially. However, Poisson's ratio becomes increasingly difficult to apply and interpret for non-cubic unit cells with higher-order symmetry or complex geometries. This limitation contributes to the strong focus on cubic unit cells in current research, despite their limited robustness due to a restricted number of symmetry axes. This study proposes volumetric strain as an alternative and geometry-independent measure of auxeticity. The approach is demonstrated through a case study on non-cubic polygon-prism unit cells generated by in-plane copy rotation. The mechanical behaviour of 2-, 4-, 6-, and 8-fold configurations is analysed using an analytical rigid-body replacement model, finite element simulations, and experimental testing. A Hoberman ring is introduced as an intermediary mechanism to enable uniform multi-directional actuation using a one-dimensional tensile tester. The results show that volumetric strain provides a consistent and robust description of auxetic behaviour across all configurations and modelling approaches. In contrast, Poisson's ratio exhibits strong sensitivity to small deviations near zero strain and leads to inconsistencies between analytical, numerical, and experimental results. The experimental force–displacement response confirms a linear scaling with the number of bases, while the volumetric strain remains independent of the initial polygonal shape of the unit cell. These findings demonstrate that volumetric strain is a reliable measure of auxeticity for non-cubic unit cells and offers clear advantages for the analysis and experimental validation of complex auxetic geometries. The proposed framework provides a foundation for extending auxetic metamaterial design towards more intricate structures, including spatially copy-rotated unit cells and honeycombs based on Archimedean solids.

1 Introduction

Auxetic metamaterials are a class of engineered materials that exhibit a negative Poisson's ratio, meaning they expand laterally when subjected to axial tension. This counterintuitive behaviour does not arise from the intrinsic properties of the base material but from the geometry of the internal structure. As such, auxetic metamaterials are a subset of mechanical metamaterials, whose effective properties are primarily governed by the architecture rather than the composition. In addition to mechanical properties, other characteristics such as acoustic [1], thermal [2], and electromagnetic [3] properties can also be tailored through geometric design. These periodic structures are typically described in terms of a *unit cell*, the smallest repeating geometric entity whose deformation behaviour defines the macroscopic response of the material. By tessellating the unit cell in two or three dimensions, complex mechanical behaviour can emerge from relatively simple local mechanisms. An auxetic unit cell is often composed of beams, hinges, or compliant segments, and is enclosed by a polygon or polyhedron known as the *honeycomb*. The honeycomb, however, is not a physical entity but rather a conceptual framework that defines how unit cells should tessellate to form a space-filling structure, ensuring the proper alignment and connectivity of adjacent cells. To organise this design space, Roberjot [4] defined six planar base families. These six base topologies can be transformed through operations such as mirroring about one or more axes and in-plane copy rotation, enabling the generation of a wide variety of auxetic unit cells. In recent years, auxetic metamaterials have garnered significant attention due to their unique mechanical properties and potential applications. They have been explored for impact absorption [5], energy dissipation [6], tunable stiffness [7], and enhanced fracture resistance [8], making them relevant for industries such as aerospace [9], medical applications [10], and protective equipment [11]. Advancements in digital fabrication, particularly 3D printing, have greatly accelerated research in this field by enabling the rapid prototyping of increasingly complex geometric designs. However, despite this progress, their practical implementation in engineering applications remains limited.

One of the key limitations is their lack of robustness. Many existing beam-based auxetic unit cells can only effectively carry loads along one of their symmetry axes, which is typically aligned with the beam geometry. Most designs found in the literature are cubic ([12–22]), which means they possess only three symmetry axes. Increasing the number of symmetry axes could improve the structural robustness and thus bring auxetic metamaterials closer to practical applications. However, the dominance of cubic designs persists because both the calculation of Poisson's ratio and experimental testing procedures become more complex as unit cells deviate from cubic symmetry [23]. Consequently, the current reliance on cubic unit cells limits the development of more robust auxetic structures.

This paper therefore proposes the use of volumetric strain as a measure of auxeticity. Unlike Poisson's ratio, the calculation of volumetric strain is independent of the geometric complexity of the unit cell. To experimentally test non-cubic unit cells, we introduce the use of Hoberman mechanisms to transform a linear actuator into a multi-directional actuation system. These experiments are compared with two models, an analytical model and finite element simulations, which allows us to identify the advantages and limitations of both measures of auxeticity. By validating the theory for copy rotation about a single axis, this study provides a foundation for

future extensions to spatial copy rotations around the centre of the unit cell, thereby lowering the barrier for exploring non-cubic auxetic metamaterials and inspiring further research into their potential applications.

In the following sections, a theoretical background on the measures of auxeticity is provided, illustrated through an example structure. This structure is analysed using three approaches: an analytical model and a finite element model for n-fold copy rotations around the z-axis, and an experimental model to test the 2-, 4-, 6- and 8-fold configurations. Each model evaluates the force–displacement curve, lateral deflection, and both measures of auxeticity. The results from these three methods are compared to assess the accuracy and validity of the models, followed by a discussion on the comparison between Poisson's ratio and volumetric strain. Finally, the extension of these methods to Archimedean solids is explored, and recommendations for future research are presented.

2 Methodology

2.1 Measure of auxeticity

Auxetic behaviour is traditionally characterised by the Poisson's ratio, which describes the relation between axial and lateral strain, with a negative value indicating auxeticity. In 2D, a single Poisson's ratio exists, relating deformation in the x- and y-directions. In 3D, two independent Poisson's ratios are required, as the third is inherently dependent on the first two. The definition is

$$\nu = -\frac{\varepsilon_{\text{lateral}}}{\varepsilon_{\text{axial}}}, \tag{1}$$

where ε denotes the strain, defined as

$$\varepsilon = \frac{L - L_0}{L_0} = \frac{\Delta L}{L_0}. \tag{2}$$

Poisson's ratio is widely used to characterise auxetic behaviour by relating axial and lateral strain, thereby describing deformation along predefined directions. In contrast, auxeticity can also be quantified using area strain in 2D or volumetric strain in 3D. These measures describe the relative change in size of a structure as a whole and are therefore independent of any specific deformation direction. These quantities are defined as:

$$\varepsilon_{\text{area}} = \frac{A - A_0}{A_0}, \tag{3}$$

$$\varepsilon_{\text{volume}} = \frac{V - V_0}{V_0}. \tag{4}$$

Because the macroscopic behaviour of the metamaterial equals that of its unit cell, both Poisson's ratio and volumetric strain can be computed at the unit-cell scale. In this work, volumetric strain is computed using the enclosing polygon prism of the unit cell, as this prism forms the tessellating element of the metamaterial. For a regular n-sided polygon with circumscribed radius r, the area is

$$A = n\, r^2\, \tan\left(\frac{180^\circ}{n}\right), \tag{5}$$

and the corresponding prism volume is

$$V = z\, n\, r^2 \tan\left(\frac{180^\circ}{n}\right), \tag{6}$$

with z the out-of-plane depth. This formulation makes it possible to evaluate the volumetric strain of any n-fold copy-rotated unit cell in a consistent and geometry-independent manner.

Although both Poisson's ratio and volumetric strain can be used to quantify auxeticity, they differ fundamentally in the type of deformation they describe and in their applicability to complex geometries. Poisson's ratio captures direction-dependent behaviour and is straightforward to evaluate for cubic, orthogonal unit cells. However, for non-cubic or higher-order symmetric structures, identifying uniquely defined axial and lateral directions becomes ambiguous, which complicates both the calculation and interpretation of Poisson's ratio. Volumetric strain, by contrast, depends only on global geometric change and therefore remains equally simple and robust to compute for all symmetry orders, at the cost of losing directional information.

2.2 Validation

The proposed use of volumetric strain as a measure for auxeticity will be verified through analytical modelling, finite-element simulations, and experimental testing. To enable a consistent comparison across structures, this study examines a set of unit cells that share the same planar auxetic base topology, referred to hereafter as the 'base', but differ in their rotational symmetry. Although the theoretical framework developed in this work can be extended to spatial copy-rotations around the centre of the unit cell, the present study focuses exclusively on copy-rotations around the z-axis. The underlying geometry of all investigated unit cells is derived from the Connected Stars base family defined by Roberjot and Herder [4]. This topology is converted into a compliant mechanism by replacing its rotational joints with flexures. The detailed embodiment process is provided in Appendix A. Using this compliant version of the base, three polygon-prism unit cells are constructed by applying 4-, 6-, and 8-fold in-plane copy-rotations. Together, these structures span a representative range of rotational symmetry orders.

Each unit cell is characterised by both its Poisson's ratio and its volumetric strain, allowing a direct comparison between the two measures of auxeticity. To ensure robust validation, every structure is examined using the three complementary approaches. The analytical model provides an initial order-of-magnitude estimate, while the finite element model offers a more accurate prediction of the force–displacement behaviour. The experimental results then serve to verify whether the FEM simulations accurately capture the actual structural response, enabling the FEM to be used with confidence for further design exploration.

2.2.1 Analytical analysis

The analytical model applied in this study is the Rigid Body Replacement Method (RBRM) [24], a model well-suited for a compliant design with small flexure lengths that experience small rotations. The flexures that serve as the revolute joints in the system are represented by notches. These notches can be effectively modelled as rotational springs with specific stiffness, as discussed by Farhadi Machekposhti et al. [24]. The joint configuration utilized in this study is a Right-Circular Corner-Filleted (RCCF) flexure hinge, as described by Chen et al. [25]. The defining relation for this hinge is expressed as follows: Let R represent half the length of the flexure, r the radius of the fillet corner, and t the thickness of the flexure. Additionally, E is the Young's modulus, b is the width of the flexure and θ is the deformation angle. The applied moment M divided by the angle θ is:

$$\frac{\theta}{M} = \frac{12}{Eb}\left(\frac{\gamma_1}{R^2} + \frac{R-r}{t^3} + \frac{\gamma_2}{r^2}\right) \tag{7}$$

where:

$$\gamma_1 = \frac{s_1^3(6s_1^2+4s_1+1)}{(2s_1+1)(4s_1+1)^2} + \frac{6s_1^4(2s_1+1)}{(4s_1+1)^{5/2}}\arctan\left(\sqrt{4s_1+1}\right) \tag{8}$$

and

$$\gamma_2 = \frac{s_2^3(6s_2^2+4s_2+1)}{(s_2+1)(4s_2+1)^2} + \frac{6s_2^4(2s_2+1)}{(4s_2+1)^{5/2}}\arctan\left(\sqrt{4s_2+1}\right) \tag{9}$$

Here, $s_1 = R/t$ and $s_2 = r/t$. Equation 7 can be re-arranged to describe the relation of M with respect to u

$$M(u) = \theta(u)\left(\frac{12}{Eb}\left(\frac{\gamma_1}{R^2} + \frac{R-r}{t^3} + \frac{\gamma_2}{r^2}\right)\right)^{-1} \tag{10}$$

Figure 1 shows the free body diagram of one base. The moments indicated in green are counteracted when the unit cell is tessellated. The two remaining moments M are intrinsic to the structure and arise from the rotational stiffness of the flexure joints. The sum of all moments must to be zero, which results in the force F as a function of the displacement u, given by:

$$\begin{aligned} \Sigma M &= 0 \\ 2M &= \frac{1}{2} F\, l \sin(\alpha) \end{aligned} \tag{11}$$

$$F(u) = \frac{4\,M(u)}{z(u)} \tag{12}$$

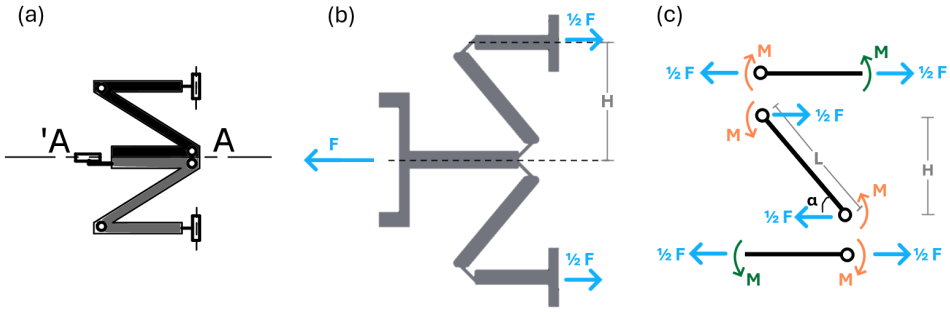

Figure 1: (a) Connected stars base from [4] (b) Free Body Diagram (FBD) of a single base (c) Simplified FBD for half of the base, where the moments shown in green are counteracted upon tessellation.

where l is the length of the arm and $\alpha(u)$ is the angle if rotation as a function of the displacement, as can be seen in Figure 1. The orthogonal component, as discussed previously, can be used to calculate Poisson's ratio between the z- and x-directions, as well as for volumetric strain. In this case, the z-value is given by:

$$z(u) = l \sin(\alpha(u)) \tag{13}$$

and for the x-direction;

$$x(u) = x_0 + u \tag{14}$$

where l is the length of the beam and α is the angle of the beam relative to the x-axis. The strain in x- and z-direction can now be calculated using α_0 for z_0 and x_0.

Using these values, both the Poisson's ratio of a single base (Equation 1) and the volumetric strain of the unit cell can be evaluated. The volumetric strain is defined as the relative change in volume, where the volume is given by the product of the polygon area A and the out-of-plane dimension z (Equations 4 and 3). Since $z(u)$ does not depend on n, the influence of the polygon geometry is fully captured by the area strain. The polygon area A and its initial value A_0 are given by Equation 5. Substituting these expressions into the area strain definition (Equation 3) yields:

$$A_0 = nr_0^2 \tan\left(\frac{180^\circ}{n}\right) \tag{15}$$

$$\epsilon_A = \frac{nr^2 \cdot \tan\left(\frac{180}{n}\right) - nr_0^2 \cdot \tan\left(\frac{180}{n}\right)}{nr_0^2 \cdot \tan\left(\frac{180}{n}\right)} \tag{16}$$

which simplifies to

$$\epsilon_A = \frac{r^2 - r_0^2}{r_0^2} \tag{17}$$

This expression shows that the area strain, and therefore the volumetric strain of the polygon-prism unit cell, is independent of the polygon order n.

The force–displacement relation for a single 'Connected stars' base, as described above, lies in the x-z plane. This base will be copy-rotated around the z-axis to create a prism polygon unit cell. Since each base is identical, the same amount of force is required to deform each one. The force is aligned with the direction of the base, and the total force required to deform an n-fold unit cell is:

$$F_{\text{total}} = n\, F_{\text{base}} \tag{18}$$

The displacement of the bases, like the force, is aligned with the direction of the base, and since all the bases exhibit identical mechanical behaviour, their displacement is uniform. To calculate the Poisson's ratio in the x-y plane, this displacement must be split across the orthogonal axes, x and y. The largest displacement values along each axis will be used to determine the Poisson's ratio. All three configurations have a Poisson's ratio of -1. This is due to the fact that Poisson's ratio uses strain rather than nominal displacement.

To establish the force–displacement relationship within all models, the Young's modulus of the material used for the prints is required. The material is PET-G; however, due to the influence of 3D printing on the Young's modulus and the inherent material variability, it is unreliable to use the typical material value. The compliant joints in the unit cells will predominantly deform in bending, making a tensile-based test inaccurate. Thus, the effective Young's modulus will be experimentally determined using cantilevers. A specially designed

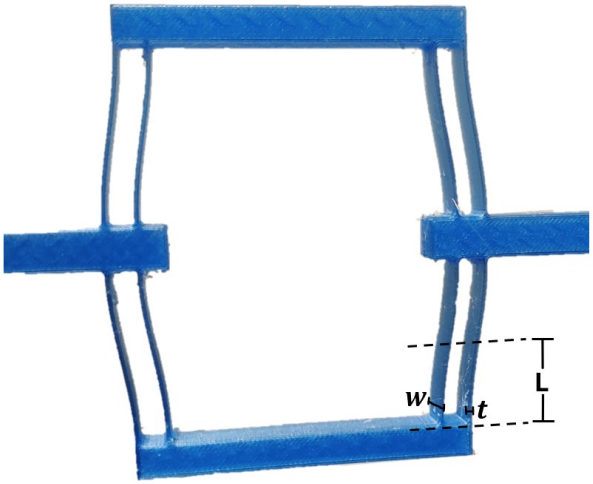

Figure 2: Cantilever plus dimensions

test specimen, consisting of sixteen identical cantilevers organised in four flexure pairs, is used for this purpose, as shown in Figure 2. This configuration offers two main advantages. First, the total displacement is amplified due to the parallel behaviour of the cantilevers, which reduces measurement inaccuracies. Second, errors due to random variations in the printing process are averaged over the sixteen cantilevers, improving the overall accuracy of the test. The test specimen is loaded in a linear tensile tester. Each cantilever deforms in bending, with effective length L, width h, and thickness b, as indicated in Figure 2. The Young's modulus is derived using the classical Euler–Bernoulli relation for a cantilever beam under a point load:

$$E = \frac{F\,L^3}{3\,u\,I} \tag{19}$$

where the moment of inertia is:

$$I = \frac{tw^3}{12} \tag{20}$$

Although the specimen contains sixteen cantilevers in total, these elements do not act independently. The cantilevers are paired to form eight flexural hinges, of which four are connected in series along the loading direction. For elements connected in series, the transmitted force is identical in each segment. Consequently, the total measured force is shared by the four flexural segments, yielding

$$F_{cl} = \frac{F_t}{4} \tag{21}$$

The measured displacement is then normalised to the displacement of a single cantilever, as two flexures, and therefore four cantilevers, are aligned in series to contribute to the total horizontal displacement, resulting in:

$$u_{cl} = \frac{u_t}{4} \tag{22}$$

The experimentally determined Young's modulus is subsequently used as a material parameter in both the analytical model and finite element simulations, enabling a comparison of the force–displacement curves from the analytical and numerical models with the experimental results.

2.2.2 Computer models

The computer models are developed using SolidWorks (version 2025), a widely used CAD software, to represent the geometries of the auxetic unit cells. The 4-, 6-, and 8-fold Connected Stars (CS) unit cells are modelled using the same parameters as those in the analytical model. The finite element analysis was carried out using COMSOL Multiphysics 6.2 (Classkit License). A stationary model was used with solid mechanics physics to simulate the deformation of the unit cells under applied displacements. A stationary model is sufficient for this analysis, as the experiments are conducted slowly, minimizing dynamic effects. For the FEM setup, a finer mesh was applied, consisting of 118,436 tetrahedral elements. The prescribed displacement, u, was applied to each

base in the direction of the base. To model the complete movement, an auxiliary sweep was used, ranging from -0.0075 m to 0.0125 m, with steps of 0.0025 m.

The applied displacement was prescribed at the end of each base, while the z-movement was constrained to zero, simulating the fixed support at the base of the unit cell. Probes were used to capture the relevant data. The first is a boundary probe, which generates the z-displacement using the expression *solid.disp* to capture the displacement at the top of the unit cell. Since the absolute value of the displacement is obtained from this expression, the compression was manually adjusted to a negative value during post-processing. The second probe measures the force required to deform the base in response to the prescribed displacement, using a surface integration probe with the expression *solid.RFx*. The resulting data from the simulations is exported to Excel, where it is processed and then imported into Python to generate the required figures and graphs for further analysis.

2.2.3 Experimental set up

All experiments are conducted in a linear tensile tester, which applies a controlled displacement to the unit cells. However, when the tensile tester is used directly on the unit cell, the structure is actuated only along a single axis. As a result, the the increased number of bases of the 4-, 6-, and 8-fold unit cells would not manifest in their deformation behaviour. To ensure uniform multi-directional actuation, a Hoberman ring is introduced as an intermediary mechanism. The Hoberman ring expands uniformly in its own plane and exhibits a Poisson's ratio of -1 over its full range of motion, making it ideally suited for the actuation of rotationally symmetric auxetic structures. Its motion is defined by scissor mechanisms arranged in a circle. Each scissor pair contains a central angle defined as:

$$\beta = \frac{360^\circ}{n} \ , \tag{23}$$

where n is the number of scissor pairs in the ring. The ring used in this study consists of 24 scissor pairs, enabling compatibility with the 4-, 6-, and 8-fold unit cells. The individual beams therefore subtend an angle of 15°.

The primary design objective of the Hoberman ring is to minimise friction so that the measured response reflects the behaviour of the unit cell, rather than artefacts of the actuation mechanism. To achieve this, each joint is constructed as a three-layer sandwich configuration, where all right-bending beams are duplicated and enclose the left-bending beam. This arrangement prevents out-of-plane moments at the joints, which would otherwise increase friction during expansion. The rotational joints are implemented using printed holes in the beams, through which thin solder-wire pins are inserted. These rods are glued into the lower layer during assembly and subsequently bonded to the upper layer after alignment. The inner joints contain orthogonal rods that support the unit cell, with the rods on the upper layer intentionally being shorter than those on the lower layer to facilitate assembly and disassembly. Two opposing mid-joints contain additional rods that allow the entire ring–unit cell system to be suspended within the tensile tester. Finally, all rods are manually sanded to reduce surface roughness after printing, ensuring that the beams of the ring can rotate freely relative to the joints. The Hoberman ring is fabricated out of PLA, a material chosen for its stiffness and low friction coefficient, making it well-suited for use in printed mechanisms where rigidity is required. In contrast, the bases of the unit cells are 3D printed from PET-G, which is ideal for compliant mechanisms due to its flexibility, durability, and ability to bend without failure. To ensure precise alignment of the bases, circular connection plates are 3D printed from PLA to maintain the correct angular spacing between the bases at both the top and bottom of the structure. These plates are then clamped together, locking the bases in place and preventing any rotational movement during testing. This mechanical locking mechanism ensures that the bases remain stationary in their desired orientation, contributing to the consistency and reliability of the experimental results. Figure 3 illustrates the test setup used in this study, with numbered labels indicating the key components of the suspension system and the arrangement of the Hoberman ring.

The tensile tester used in this study operates in an upright configuration. A horizontal setup was avoided because the large span of the Hoberman ring could cause sagging due to its self-weight, which would interfere with the uniform in-plane motion of the structure. The Hoberman ring is mounted inside the vertical tensile tester using suspension supports. These supports are clamped into the tensile tester and feature extended beams to ensure that the clamping mechanism does not interfere with the movement of the Hoberman ring. At the end of these extended beams, holes are placed where the rods from the ring fit in, allowing for secure attachment. The beams are further supported by angled beams at the base to maintain stability during operation.

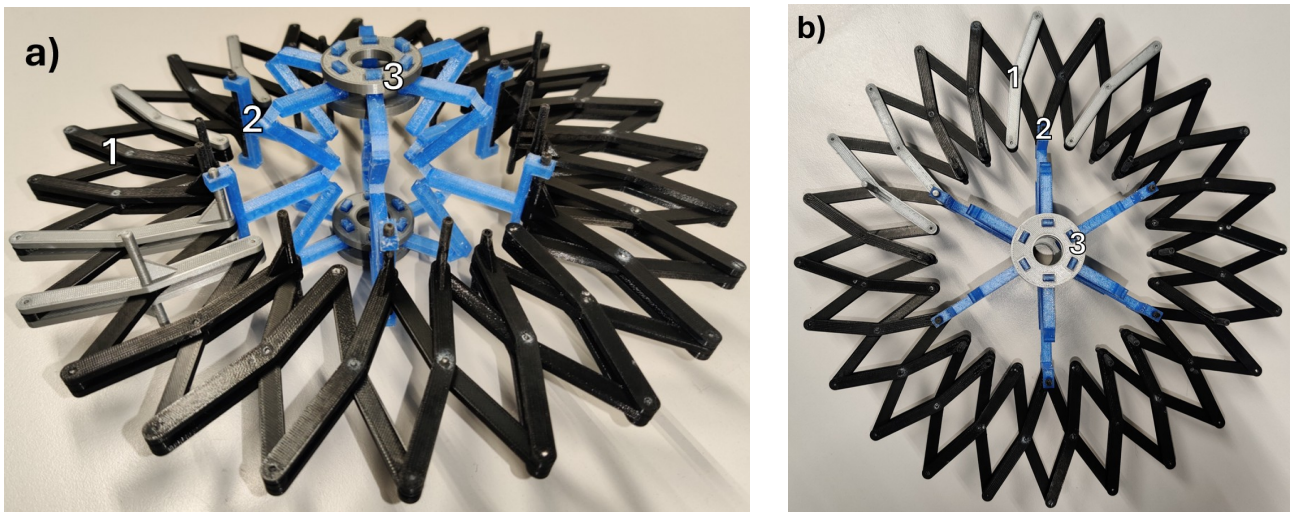

Figure 3: Test setup showing (a) the side view and (b) the top view. The numbered elements indicate (1) the Hoberman ring, (2) the connection between the unit cell and the Hoberman ring, and (3) the connection plates.

To evaluate the influence of the Hoberman ring on the force–displacement response, a series of tests is conducted. A 2-fold (2F) unit cell is used as a reference configuration, as it is inherently planar and can therefore be tested both with and without the Hoberman ring. Comparing these two sets of measurements allows the additional force contribution of the ring to be quantified. In addition, the Hoberman ring is tested without a unit cell to obtain a force–displacement curve over a larger range than in the experimental setup. This provides insight into the inherent resistance of the mechanism and its overall effectiveness as an actuation system. However, the behaviour of the ring can depend on how it is loaded. When actuated in isolation, its deformation pattern differs from the loading condition imposed when a unit cell is attached. For this reason, the 2F reference configuration provides a more reliable estimate of the ring-induced force contribution than the ring-only test. The 4-, 6-, and 8-fold unit cells are subsequently tested following the same procedure. For each configuration, the first test run is discarded, as the structure requires one full actuation cycle to settle into its deformation pattern. After this settling cycle, three consecutive tests are performed to assess the mechanical response and its repeatability. All tests are conducted at a low actuation speed to minimise the influence of hysteresis. Finally, the cantilever specimen described in Section 2.2.1, used for the experimental determination of the Young's modulus, is also tested. Similar to the unit-cell tests, the first run is disregarded, and at least two additional runs are conducted to ensure the results are consistent and reproducible.

The tensile tester records the force–displacement data during each experiment. To capture the displacement corresponding to the z-value used in the analytical and numerical models, which aligns with the global horizontal direction in the vertical test set-up, additional visual data is collected through video tracking. A red marker is placed on both the top and bottom clamping plates of the unit cell, allowing their relative movement to be tracked using the video analysis software Kinovea. The visual recordings are obtained using a OnePlus 7T Pro smartphone equipped with a 48-megapixel camera. The smartphone is mounted on a fixed tripod, and its position remains unchanged throughout all experiments to ensure consistent camera perspective and measurement conditions.

To enable the comparison across all three models, several post-processing steps are required for the experimental results. The force–displacement data from the experiments is processed in four stages:

1. The average of the three repeated tests is taken to reduce the influence of random fluctuations and to obtain a representative force–displacement curve.

2. If the Hoberman ring not only contributes friction but also stiffness, this stiffness will be subtracted from the measurements. This will be determined using the results from the empty ring and the 2F reference configuration.

3. The displacement applied at the middle joint, where the ring is suspended from the linear actuator, is converted to the displacement at the inner joint of the ring, where the unit cell is fixed. This conversion allows for the correct measurement of the unit cell's displacement.

4. Normalization per base: the corrected total force is divided by the number of bases of the unit cell, yielding a force–displacement curve for a single base. The converted displacement is then divided by two, resulting in the displacement corresponding to a single base.

The displacement in z-direction is obtained from the video recordings through motion tracking in Kinovea (version 2024.1.1). In Kinovea, two tracking points are placed on the red markers located on the top and bottom plates of the unit cell. The software provides linear kinematic outputs, including horizontal and vertical displacement. In the vertical test set-up, the horizontal displacement corresponds to the model's z-value. To ensure accurate output, Kinovea requires the definition of a reference length. This calibration is performed using an object positioned at the same depth relative to the camera to avoid distortion caused by depth differences. The only available feature at this depth is the width of the circular connection plate (indicated as 5 in Figure 6), which is 4 mm. This short reference length is sensitive to calibration errors, as it is of the same order of magnitude as the measured displacements. Any inaccuracy in defining the length on the calibration line directly and proportionally affects all recorded displacement values. To verify the reliability of the calibration, the vertical displacement extracted from Kinovea is compared with the displacement imposed by the tensile tester. For each test, the tracking is repeated if the deviation exceeds 5%. The resolution and step size of the software introduce a degree of measurement noise. For each test, the data is taken from the starting position, through compression, then extension, and back to zero. To process the data, the first and last portions (from and to zero) are disregarded, and only the data between the two extremes is considered. This data is then normalised to the extremes of the displacement in x direction to ensure consistency. Finally this data will be approximated using a second order polynomial regression, to filterout the measurement noise. In addition, to minimise random error, the average is taken from both sides of the displacement and across all three runs per configuration, resulting in an average of six curves per configuration.

Once the z-value is established, the Poisson's ratios and volumetric strain are computed in Excel and Python using Equations 1, 6 and 4. To ensure an equal comparison between all three models, the analytical and FE models are both approximated with a second-order polynomial also.

3 Results

3.1 Young's modulus

The Young's modulus is determined from the test results shown in Figure 4, using Equations 19 and 20. Data points at 0.5 mm and 9.5 mm of displacement are selected to avoid any artefacts associated with the initial settling phase and the reversal of the load. The difference in force between these two points, combined with the corresponding difference in displacement, yields a Young's modulus of $E = 1.84\,GPa$. This value is of the same order of magnitude as the material properties provided by the manufacturer of the PET-G filament. Although a full loading–unloading cycle was recorded, no visible hysteresis is observed in the force–displacement curve. This behaviour is likely the result of the very low testing rate of 20 mm/min, which was selected to minimise hysteresis effects.

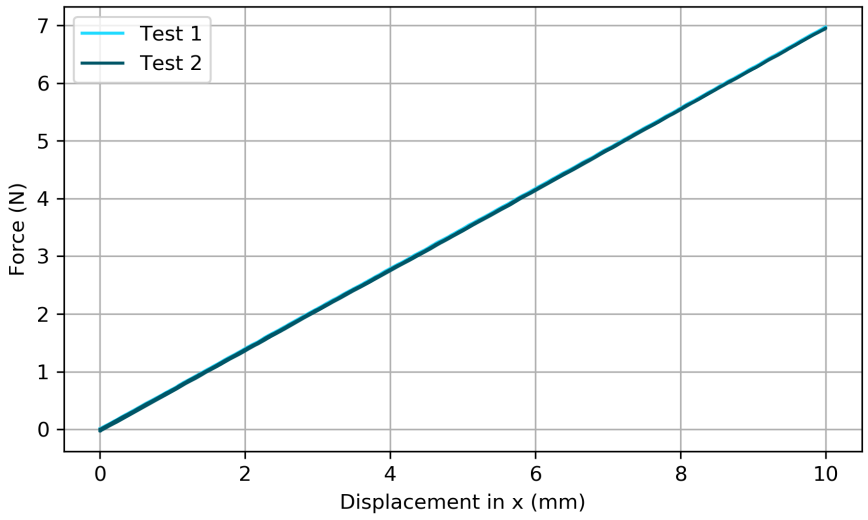

Figure 4: Force–displacement results of the cantilever specimen over two full loading–unloading cycles.

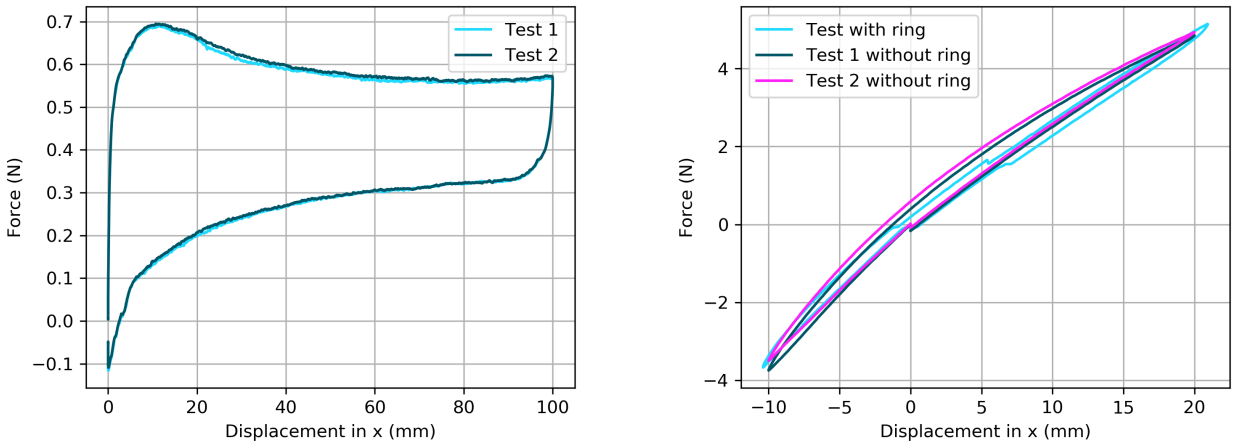

(a) (b)

Figure 5: Force–displacement results of (a) the Hoberman ring without a unit cell and (b) the 2-fold reference test with and without the Hoberman ring.

3.2 Hoberman ring

The Hoberman ring was first tested without a unit cell to characterise its inherent force–displacement behaviour. The results, shown in Figure 5a, indicate that the measured force is slightly higher within the first 40 mm of displacement. In this region, the mechanism is in its collapsed state, meaning that the angle between the right-bending and left-bending beams is very small and the contact area around the joints is large. This results in a slightly larger separation between the extension and compression paths of the curve. Beyond this initial phase, the ring transitions into the mid-range of its total expansion span, where the regions of overlap become smaller. As the maximum expansion of the ring exceeds 350 mm, the displacement range used in all unit-cell experiments (60–80 mm) lies well within this stable mid-range region. Here, the frictional resistance is consistent, and the force–displacement response becomes nearly flat. This behaviour confirms that the ring itself does not introduce measurable stiffness, which could have occurred if there were alignment issues. Across this stable operating range, the friction associated with the actuation mechanism remains very low, requiring less than 0.6 N to expand the entire ring.

Figure 5b shows the comparison between the 2-fold configuration tested with and without the Hoberman ring. The curve obtained with the ring displays a slightly larger deformation range due to the post-processing conversion described in Section 2.2.3. A noteworthy and unexpected observation is that the test with the ring requires less force to deform than the test without the ring, and the amplitude between the load and unload curves appears to be smaller in the test with the ring. Since the Hoberman ring introduces friction, one would expect it to increase the amplitude between these curves in the test with the ring. However, these discrepancies are likely due to differences between the bases used in the two tests. Small variations can arise from random printing imperfections or from the accumulated wear of bases that have been tested previously, which could also affect the hysteresis behaviour of the bases. As the trend in all three measurements is consistent and the test with the empty ring shows a flat force–displacement curve, it can be concluded that the Hoberman ring does not contribute any significant stiffness to the system. For this reason, no correction for the ring force will be applied in the subsequent analyses, as the additional contribution of the Hoberman mechanism is negligible compared to the variability between the printed bases.

3.3 Force displacement curves

The force–displacement curves for each configuration are shown in Figure 7, while an overview of the experimental test setup is provided in Figure 6. In all four cases, the curves for the three runs align so closely that it is barely noticeable that multiple tests are plotted, indicating a highly repeatable mechanical response. However, small irregularities appear in the curves, most notably near zero force. These irregularities arise from slight play in the suspension, which caused minor perturbations when the linear tensile tester transitioned from compression to expansion.

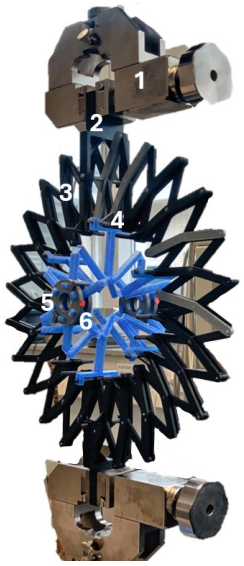

Figure 6: Test setup with (1) attachment of the linear tensile tester, (2) suspension system, (3) Hoberman ring, (4) connection of the unit cell to the Hoberman ring, (5) connection plate, and (6) tracking marker.

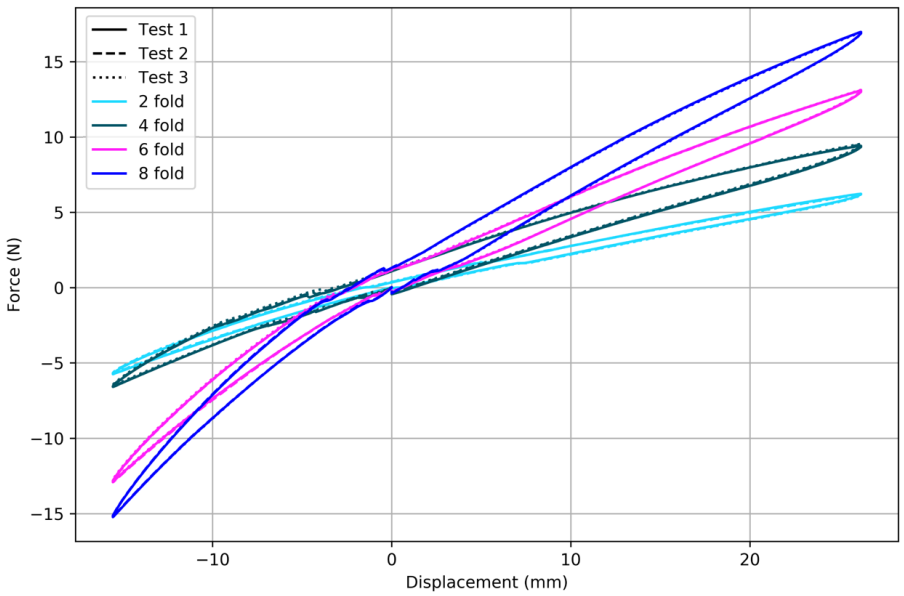

Figure 7: Force–displacement results for 2-, 4-, 6-, and 8-fold unit cells, showing three full loading–unloading cycles per configuration.

In Figure 8, the force–displacement curves obtained from the three modelling approaches are compared. All models show a similar overall shape, with a steeper response in compression than in extension. Although the qualitative behaviour is comparable, the analytical and finite element models predict force levels that are more than twice those measured experimentally. This behaviour is primarily due to the inherent geometry of the structure, where α governs the mechanical response. Notably, the experimental displacement range extends from -7.78 mm to 13.1 mm, in contrast to the -7.5 mm to 12.5 mm range observed for the other two models. This difference is attributable to the radius conversion discussed in Section 2.2.3. The normalized data from the experiments is shown in Figure 8, where all four configurations yield highly comparable results. The 2F configuration shows a somewhat larger deviation. This is likely due to the previously discussed variation in stiffness between individual bases. In higher-order copy rotations, this random variation is distributed over a greater number of bases, resulting in a more uniform response. Furthermore, although the effect of the Hoberman ring could not be reliably isolated using the 2F reference test, this does not imply that the influence is absent. Any residual contribution from the ring may still play a minor role in the small discrepancies observed between the unit cells of different rotational symmetry orders, as this contribution is also divided by the number of bases.

3.4 Orthogonal displacement

In Kinovea, the accuracy of the calibration was verified using the vertical displacement and, if necessary, the tracking was repeated, as described in Section 2.2.3. In practice, it was never necessary to repeat the tracking. The software allows for a ten-fold zoom, enabling the calibration line to be placed with high precision. Furthermore, the calibration remains consistent when new videos are processed, meaning that all tracking was performed using the same calibration settings. This ensures full consistency across the twelve tests (three runs for each of the four configurations). Figure 9 shows an example of the raw displacement data obtained from the visual tracking. A step-like noise pattern is clearly visible in the measurements. Additionally, some of the graphs exhibit a slight drift towards the end of the recording, where the displacement returns to approximately 0.5 mm instead of zero. This drift effect is inversely proportional to the displacement measurement on each side. This drift effect is mitigated by averaging the data from both the left and right sides of each measurement. These effects highlight the importance of using the mean of six data sets per configuration (two sides, three runs) to minimise random error. To reduce measurement noise, a second-order polynomial function is fitted to

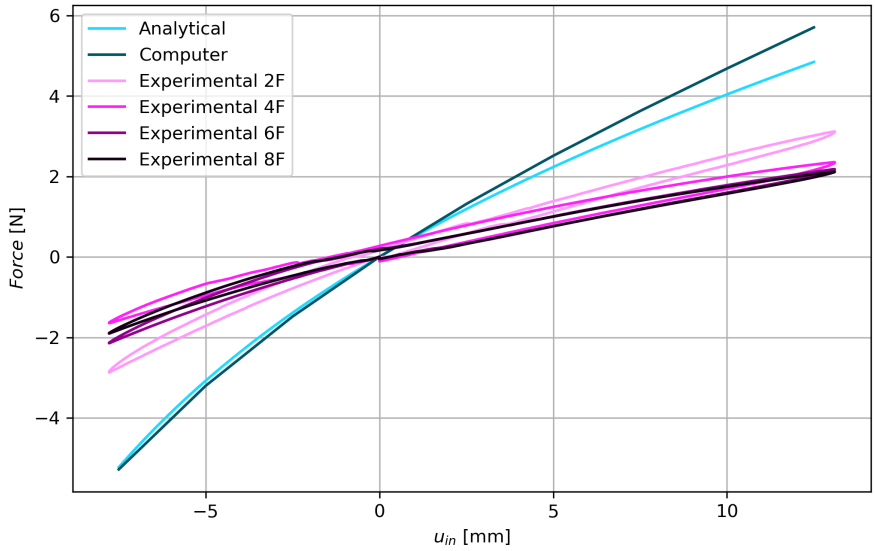

Figure 8: Force-displacement results of the analytical, computer and experimental models.

each tracking curve during the post-processing stage. Despite these small artefacts, the overall displacement trend is accurately captured.

The outcome of the processed data is shown in Figure 10. The fitted lines should ideally pass through the origin, as there should be no displacement in the z-direction when no displacement is imposed along the x-direction. All of the curves are very close to this point, indicating that there is no significant systematic error. This suggests that the chosen method of post-processing the experimental data is valid and reliable. Both the analytical model and the finite element model are fitted with a second-order polynomial to ensure

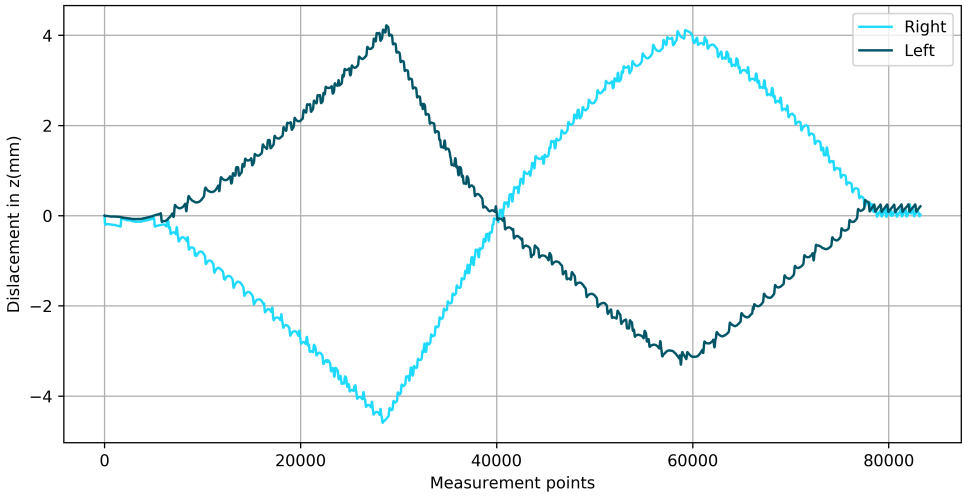

Figure 9: Raw displacement data obtained from motion tracking for the 2-fold configuration (test 1).

that the results are as comparable as possible. The results of all models are shown in Figure 10 with a dashed line that indicates the approximation. The deviations between the polynomial fits and the models are minimal. The results from the FEM and experimental tests are very similar. However, the analytical model exhibits deflections nearly twice the size of those observed in the FEM and experimental results, despite having the same overall shape. This discrepancy arises from the definition of the analytical model, particularly the length of the beam.

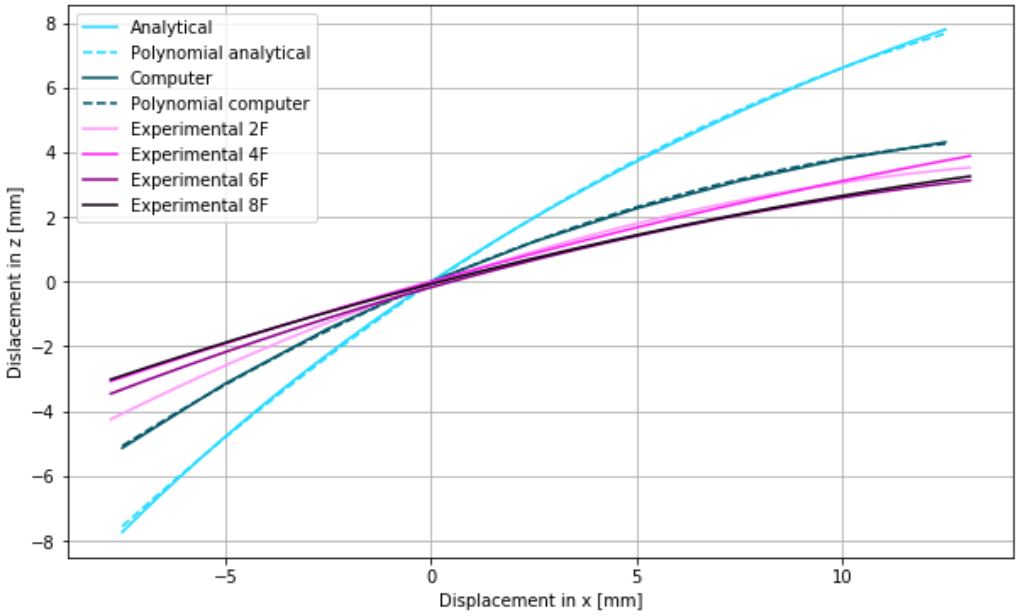

Figure 10: Z displacement and 2nd order polynomial approximation of the analytical, computer and experimental models.

3.5 Poisson's ratio

The polynomial approximation does not perfectly pass through the origin, resulting in pronounced peaks in the displacement data near zero deflection, as shown in Figure 11. This issue arises from the calculation of Poisson's ratio (Equation 1), which involves dividing two strain components. Even small nominal differences between these strains can lead to disproportionately large discrepancies, as the strains can differ by an order of magnitude near zero. To mitigate the impact of these distortions, data points near zero displacement are excluded during post-processing. For the 6F and 8F configurations, more extensive exclusion of data points is required, whereas the 4F configuration shows a particularly clean response. In terms of displacement values, the analytical model predicts a relatively large z-displacement for the same input, which aligns with the higher Poisson's ratio observed in the experimental results.

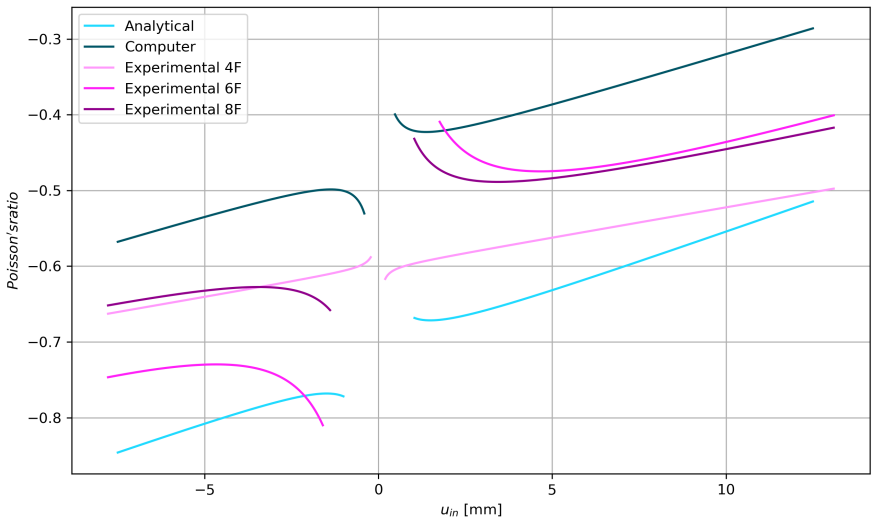

Figure 11: Poisson's ratios from the analytical, finite element, and experimental models.

3.6 Volumetric strain

Figure 12 shows that the results from all three models follow the same trend, and the values do not differ significantly. However, the analytical model yields slightly higher results, which accurately capture the behaviour in the z-displacement. The experimental results also show a high degree of consistency. In this case, no artifacts are observed, as the approximations do not need to pass through the origin perfectly.

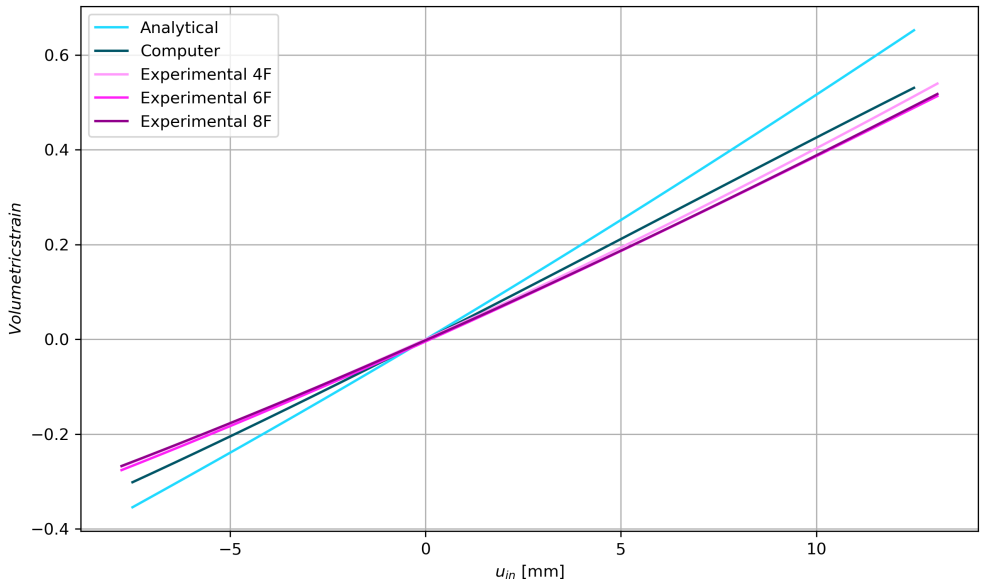

Figure 12: Volumetric strain from the analytical, finite element, and experimental models.

4 Discussion

One of the key motivations for this study was the lack of research into non-cubic unit cells, primarily due to the difficulty in calculating their behaviour and the challenges of testing such structures. The Hoberman ring has proven to be an effective tool for testing unit cells with polygon prism honeycombs, enabling a 1D actuator to apply multi-directional deformation reliably. The results show that the Hoberman ring performs well under the test conditions, accurately capturing the mechanical response without significant interference. This consistent performance underscores the potential of the Hoberman ring for experimental setups in testing auxetic structures.

As expected, the total force required for deformation increases linearly with the addition of each base. The experiments show a clear linear relationship between the number of bases and the total force. However, the 2F configuration shows a slight deviation from this trend. This discrepancy is likely due to a stiffer base, which could result from random printing errors or an increase in stiffness due to prior testing. Although this variation was minimal and did not significantly impact the overall results, it highlights the importance of consistent manufacturing techniques when performing such tests.

The analytical and finite element models predict force levels that are more than twice those obtained from the experiments. The origin of this discrepancy could not be determined within the scope of the present study. Possible contributing factors include variations introduced during the 3D printing process, such as geometric inaccuracies or local differences in material behaviour, as well as the potential onset of plastic deformation during repeated testing. These effects were not examined in detail in this work. Further investigation is therefore required to identify the dominant mechanisms and to improve the accuracy of the predicted force–displacement response.

The approximated values for Poisson's ratio show discrepancies between the models, as well as inconsistencies between the experimental results themselves. While the analytical model is expected to yield larger values due to the increased z-displacement, this aligns with the expectation that a larger displacement should result in a higher Poisson's ratio. However, even though the finite element model and experimental results show very similar

z-displacements, a notable difference in Poisson's ratio remains. This, along with the discrepancies observed near zero displacement, suggests that Poisson's ratio is highly sensitive to small measurement differences, making it an unreliable indicator of auxeticity in certain cases.

In contrast, the volumetric strain method produced three curves with similar overall shapes, as observed in the other results of this study. The variations in the values for volumetric strain also correspond well with the observed z-displacement values. As expected, the analytical model yields the highest value, with the finite element model and experimental results closely matching each other. This demonstrates that volumetric strain accurately captures the behaviour of the unit cells, providing a more robust and consistent measure of auxeticity than Poisson's ratio.

The calculations for these configurations are of similar complexity, as the copy rotations occur around a single axis. However, as the structure becomes more intricate with spatial copy rotations around the centre, or a combination of different bases, calculating Poisson's ratio becomes more challenging. This arises from the need to project the contribution of each base onto the spatial axes, complicating the calculation. In contrast, the formula for volumetric strain remains simple, as it is based on the volume of the unit cell, which depends on just one or two variables. These variables are the input and output displacements, both of which are known or measurable. No additional calculation steps are required, even when the unit cell becomes more complex.

This simplicity makes volumetric strain ideal for auxetic unit cells with the shapes of Archimedean solids. Archimedean solids are a group of 13 convex polyhedra, where each face is a regular polygon and each vertex is surrounded by the same set of polygons. These solids are particularly interesting because they can be arranged to fill space in various configurations, known as tessellations. There are several space-filling configurations possible with Archimedean solids, as described in Appendix C. An auxetic metamaterial based on one of these configurations could be more robust, as it has more symmetry planes. For example, number 5 of Appendix C a combination of the Great Rhombcuboctahedron, the Truncated Tetrahedron, and the Truncated Cube provides 13 symmetry axes, compared to the 3 of a cubic structure. Thus, volumetric strain offers a more straightforward and reliable measure of auxeticity in these cases, making it a valuable tool for further research into non-cubic unit cells and, consequently, more robust metamaterials.

However, volumetric strain is a single parameter, whereas Poisson's ratio involves two independent ratios. Therefore, some directional information is inherently lost when using volumetric strain alone. To compensate for this loss of directionality, the kinematic behaviour of one base should be studied. Combined with the shape of the unit cell and the volumetric strain, this approach provides a more comprehensive understanding of the directionality of deformation than Poisson's ratio alone.

The z-displacement results indicate that the analytical model deviates from the numerical and experimental models. This deviation is mainly related to the simplifying assumptions required to obtain a tractable analytical description. In the analytical formulation, the structure is idealised as a system of rigid beams connected by rotational springs, which does not fully capture the geometric details of the physical configuration. A contributing factor to this deviation is the definition of the effective beam lengths used in the analytical model. The initial formulation approximates the geometry as z-shaped mechanism, which results in an overestimation of the vertical displacement. To address this, the analytical geometry was refined by shortening the inclined beam segments and introducing two vertical segments to maintain the overall height of the structure. This adjustment provides a closer representation of the deformation path while preserving the analytical framework. The refined analytical model is described in Appendix C, where a schematic representation is shown in Figure 16. The corresponding z-displacement results are presented again in Figure 17. Although the revised model reduces the discrepancy, the analytical predictions still overestimate the observed response.

The analytical model can be extended to different base families as defined by Roberjot [4], providing a simple and effective first step in analysing a broader range of auxetic structures. By adjusting the characteristics of the base and the definition of the symmetry lines, which may vary depending on the configuration, the model can be easily adapted to different setups, allowing for quick variations in parameters to achieve the desired results. This approach offers valuable insight into the mechanical behaviour of the system, as demonstrated in this study. The simplicity of the analytical model means that researchers can avoid the need for complex 3D CAD models in the early stages of design, making it a practical tool for obtaining a preliminary understanding of how the system will behave.

The analytical model can be extended to different base families as defined by Roberjot [4], providing a simple and effective first step in analysing a broader range of auxetic structures. The free body diagrams and corresponding force–moment relations for these base families are summarised in Appendix B, where the mechanical formulation of each topology is presented explicitly. By adjusting the characteristics of the base and the definition of the symmetry lines, which may vary depending on the configuration, the model can be readily adapted to different setups. This enables rapid parameter variation to explore the mechanical response without the need for full three-dimensional modelling. As demonstrated in this study, this approach provides valuable

insight into the mechanical behaviour of the system at an early design stage. The simplicity of the analytical model allows researchers to avoid complex 3D CAD and finite element models during initial exploration, making it a practical and efficient tool for preliminary design assessment.

Lastly, transitioning from planar bases to spatial bases would also be of significant interest. This transition opens up a wider range of possible configurations as the base topology shifts from planar to spatial, an example of which is illustrated in Appendix D. With multiple-order copy rotations, both within a single base and between bases around the centre of the unit cell, volumetric strain becomes an increasingly convenient measure for describing these structures, as the calculation of Poisson's ratio becomes highly complex. Such a shift could significantly impact the performance and deformation of the unit cells, particularly in hierarchical auxetic structures.

5 Conclusion

In this study, volumetric strain is proposed as an alternative measure of auxeticity to the commonly used Poisson's ratio. It is shown that volumetric strain is particularly well suited for describing experimental results and approximations of real-world systems, as it does not require all deformation components to reach zero exactly at the same instance. This makes it less sensitive to small deviations that are inherent to experimental measurements and numerical approximations.

Furthermore, this study demonstrates that a Connected Stars–based unit cell, copy-rotated n times about the z-axis, can be accurately described using both an analytical model and a finite element model. Experimental testing of the 4-, 6-, and 8-fold configurations using a Hoberman ring further supports the validity of these models. The 2-fold reference experiments confirm that the Hoberman ring provides an effective means of converting a one-dimensional imposed displacement into a uniform multi-directional actuation. In addition, the ring introduces only minimal stiffness and friction, ensuring that the measured force–displacement relations accurately reflect the mechanical response of the unit cells.

Both the concept of volumetric strain and the experimental assessment using Hoberman mechanisms can be extended to more intricate structures, including unit cells with spatial rather than planar bases, as well as configurations based on Archimedean solids instead of polygon prisms. Variations in base geometry and stiffness can be incorporated without increasing the complexity of the volumetric strain formulation. In these cases, volumetric strain becomes increasingly advantageous, as the complexity of its calculation increases much less significantly than that of Poisson's ratio, particularly when the base lengths differ or when the bases directions do not align with the axes of a Cartesian coordinate system. This approach lays the foundation for a substantial expansion the design space of auxetic materials. In particular, honeycombs based on Archimedean solids offer a larger number of symmetry axes, which may enhance structural robustness and bring auxetic metamaterials closer to practical engineering applications

References

[1] Xiyue An et al. "3D acoustic metamaterial-based mechanical metalattice structures for low-frequency and broadband vibration attenuation". In: *International Journal of Solids and Structures* 191-192 (2020), pp. 293–306. ISSN: 0020-7683. DOI: 10.1016/j.ijsolstr.2020.01.020.

[2] Xiaoyue Ni et al. "2D Mechanical Metamaterials with Widely Tunable Unusual Modes of Thermal Expansion". en. In: *Advanced Materials* 31.48 (2019), p. 1905405. ISSN: 1521-4095. DOI: 10.1002/adma.201905405.

[3] Maria Sakovsky, Jan Negele, and Joseph Costantine. "Electromagnetic Reconfiguration Using Stretchable Mechanical Metamaterials". en. In: *Advanced Science* 10.6 (2023), p. 2203376. ISSN: 2198-3844. DOI: 10.1002/advs.202203376.

[4] Pierre Roberjot and Just L. Herder. "A unified design method for 2D auxetic metamaterials based on a minimal auxetic structure". en. In: *International Journal of Solids and Structures* 295 (2024), p. 112777. ISSN: 00207683. DOI: 10.1016/j.ijsolstr.2024.112777.

[5] Jianlin Zhong et al. "Mechanical behaviors of composite auxetic structures under quasi-static compression and dynamic impact". In: *European Journal of Mechanics - A/Solids* 109 (2025), p. 105454. ISSN: 0997-7538. DOI: 10.1016/j.euromechsol.2024.105454.

[6] Ramin Hamzehei et al. "3D-printed bio-inspired zero Poisson's ratio graded metamaterials with high energy absorption performance". en. In: *Smart Materials and Structures* 31.3 (2022). Publisher: IOP Publishing, p. 035001. ISSN: 0964-1726. DOI: 10.1088/1361-665X/ac47d6.

[7] Xian Cheng et al. "Design and mechanical characteristics of auxetic metamaterial with tunable stiffness". In: *International Journal of Mechanical Sciences* 223 (2022), p. 107286. ISSN: 0020-7403. DOI: 10.1016/j.ijmecsci.2022.107286.

[8] Jianjun Zhang, Guoxing Lu, and Zhong You. "Large deformation and energy absorption of additively manufactured auxetic materials and structures: A review". In: *Composites Part B: Engineering* 201 (2020), p. 108340. ISSN: 1359-8368. DOI: 10.1016/j.compositesb.2020.108340.

[9] A. Airoldi et al. "Design of a morphing airfoil with composite chiral structure". In: *Journal of Aircraft* 49.4 (2012), pp. 1008–1019. DOI: 10.2514/1.C031486.

[10] Mohammad Sadegh Ebrahimi et al. "Revolutionary auxetic intravascular medical stents for angioplasty applications". In: *Materials & Design* 235 (2023), p. 112393. ISSN: 0264-1275. DOI: 10.1016/j.matdes.2023.112393.

[11] Mohammad Sanami et al. "Auxetic Materials for Sports Applications". In: *Procedia Engineering*. The Engineering of Sport 10 72 (2014), pp. 453–458. ISSN: 1877-7058. DOI: 10.1016/j.proeng.2014.06.079.

[12] T. Bückmann et al. "Tailored 3D mechanical metamaterials made by dip-in direct-laser-writing optical lithography". In: *Advanced Materials* 24.20 (2012), pp. 2710–2714. DOI: 10.1002/adma.201200584.

[13] X. Fang, H.-S. Shen, and H. Wang. "Three-point bending behaviors of sandwich beams with data-driven 3D auxetic lattice core based on deep learning". In: *Composite Structures* 354 (2025). DOI: 10.1016/j.compstruct.2024.118751.

[14] D. Faraci, L. Driemeier, and C. Comi. "Bending-Dominated Auxetic Materials for Wearable Protective Devices Against Impact". In: *Journal of Dynamic Behavior of Materials* 7.3 (2021), pp. 425–435. DOI: 10.1007/s40870-020-00284-2.

[15] B. He, Q. Huang, and Z. Shi. "A novel three-dimensional orthogonal star honeycomb structure with negative Poisson's ratio". In: *Engineering Research Express* 6.1 (2024). DOI: 10.1088/2631-8695/ad337d.

[16] C. Li, H.-S. Shen, and H. Wang. "Postbuckling behavior of sandwich plates with functionally graded auxetic 3D lattice core". In: *Composite Structures* 237 (2020). DOI: 10.1016/j.compstruct.2020.111894.

[17] K.K. Dudek et al. "Micro-Scale Auxetic Hierarchical Mechanical Metamaterials for Shape Morphing". In: *Advanced Materials* 34.14 (2022). DOI: 10.1002/adma.202110115.

[18] N. Feng et al. "A novel 3D bidirectional auxetic metamaterial with lantern-shape: Elasticity aspects and potential for load-bearing structure". In: *Composite Structures* 321 (2023). DOI: 10.1016/j.compstruct.2023.117221.

[19] C.Q. Lai, K. Markandan, and Z. Lu. "Anomalous elastic response of a 3D anti - tetrachiral metamaterial". In: *International Journal of Mechanical Sciences* 192 (2021). DOI: 10.1016/j.ijmecsci.2020.106142.

[20] T. Li and Y. Li. "3D Tiled Auxetic Metamaterial: A New Family of Mechanical Metamaterial with High Resilience and Mechanical Hysteresis". In: *Advanced Materials* 36.15 (2024). DOI: 10.1002/adma.202309604.

[21] Z. Li et al. "3D Printing of Auxetic Shape-Memory Metamaterial towards Designable Buckling". In: *International Journal of Applied Mechanics* 13.1 (2021). DOI: 10.1142/S1758825121500113.

[22] W. Lv, L. Dong, and D. Li. "A novel metamaterial with individually adjustable and sign-switchable Poisson's ratio". In: *European Journal of Mechanics, A/Solids* 97 (2023). DOI: 10.1016/j.euromechsol.2022.104851.

[23] B.A. Rogers et al. "Optimization and experimental validation of 3D near-isotropic auxetic structures". In: *Materials and Design* 229 (2023). DOI: 10.1016/j.matdes.2023.111844.

[24] Davood Farhadi, N. Tolou, and Just Herder. "A Review on Compliant Joints and Rigid-Body Constant Velocity Universal Joints Toward the Design of Compliant Homokinetic Couplings". In: *Journal of Mechanical Design* 137 (2015), p. 032301. DOI: 10.1115/1.4029318.

[25] Gui-Min Chen, Jian-Yuan Jia, and Zhi-Wu Li. "Right-circular corner-filleted flexure hinges". In: *IEEE International Conference on Automation Science and Engineering, 2005.* ISSN: 2161-8089. 2005, pp. 249–253. DOI: 10.1109/COASE.2005.1506777.

[26] Branko Grünbaum. "UNIFORM TILINGS OF 3-SPACE". en. In: *Geombinatorics* 4 (1994), pp. 49–56.

[27] *Archimedean Solid – from Wolfram MathWorld.*

A Appendix A

The geometric parameters of the compliant unit cell were determined experimentally. Rather than targeting a specific stiffness, the primary design objective was to identify a parameter set that ensured reliable elastic behaviour of the flexures. Specifically, the flexures needed to be sufficiently thick and short to prevent cracking caused by excessive local strains, while remaining slender enough to avoid plastic deformation during repeated actuation.

Initial test prints were performed on a single two-dimensional unit cell to evaluate suitable flexure dimensions. Three variants were produced: a baseline configuration with a flexure thickness of 1.0 mm and a length of 3.1 mm, a slender configuration with the same thickness but an increased flexure length of 4.6 mm, and a stiffer configuration with an increased thickness of 1.5 mm and a flexure length of 3.1 mm. These initial tests revealed that variations introduced by the 3D printing process had a significant influence on the mechanical response, making it difficult to reliably assess the flexure behaviour in isolation.

To reduce the influence of local printing artefacts, the test geometry was expanded to a 2×2 tessellation of the unit cell. This configuration provides a more representative deformation pattern and averages out local stiffness variations. To minimize the effects of the boundary conditions due to the suspension, a pair of leaf flexures was added on both sides of the suspension system. This system connects the tessellated structure to the linear actuator and acts as a linear slider mechanism. The resulting test setup is shown in Figure 13.

Among the tested configurations, the least stiff flexure design exhibited the most favourable behaviour. It remained fully elastic throughout the deformation range, showed no signs of plastic deformation, and allowed for smooth, repeatable motion. Based on these observations, the final geometric parameters adopted in this study are:

- flexure thickness: 1.0 mm,
- inner flexure length: 4.6 mm,
- inner arc radius: 0.25 mm.

In contrast, the beams connecting the flexures were designed to be significantly stiffer than the compliant joints, such that they could be considered rigid in comparison. This condition was successfully achieved by making the beams 6 mm thick, ensuring that the deformation of the unit cell is dominated by flexural rotation at the joints, consistent with the assumptions made in the analytical and numerical models.

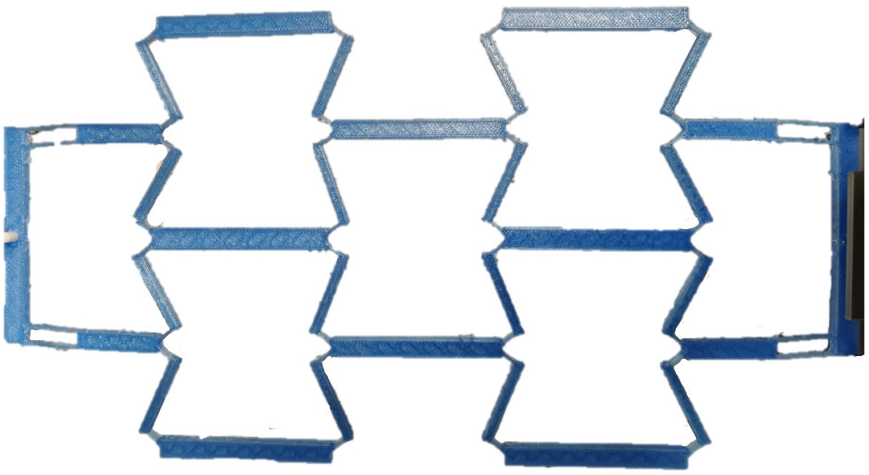

Figure 13: Two by two tessellation to asses the functionality of the parameters

B Appendix B: Analytical FBD for Auxetic Base Families

Configuration	Full cell	Free Body Diagram	Relations
Connected Stars	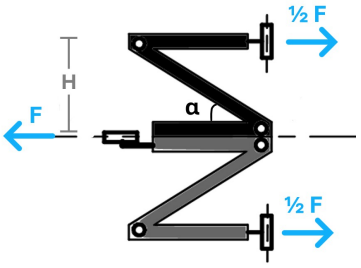	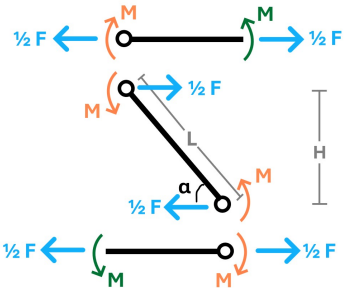	$H = \sin(\alpha)\, L$ $2\,M = (\frac{1}{2}F)\, H$ $F = \dfrac{4\,M}{\sin(\alpha)\, L}$
Puzzle Tile	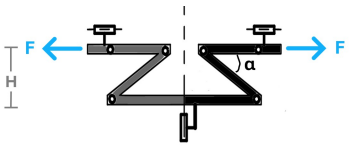	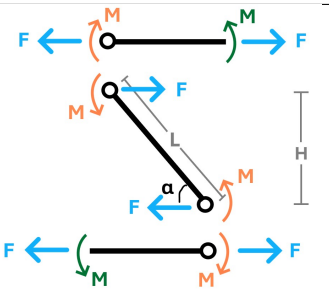	$H = \sin(\alpha)\, L$ $2\,M = F\, H$ $F = \dfrac{2\,M}{\sin(\alpha)\, L}$
Rotating Triangles	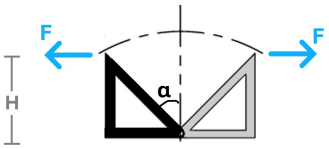	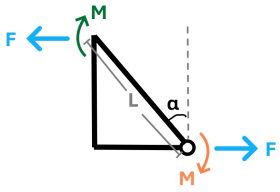	$H = \cos(\alpha)\, L$ $M = F\, H$ $F = \dfrac{M}{\cos(\alpha)\, L}$
Honey Comb	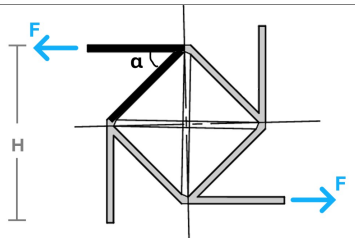	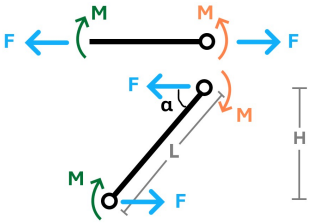	$H = 2\sin(\alpha)\, L$ $M = F(\frac{1}{2}H)$ $F = \dfrac{M}{\sin(\alpha)\, L}$
Missing Rib	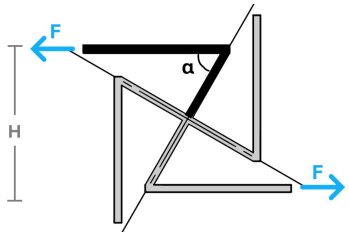	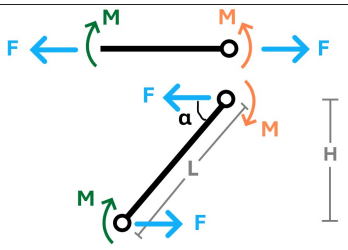	$H = 2\sin(\alpha)\, L$ $M = F(\frac{1}{2}H)$ $F = \dfrac{M}{\sin(\alpha)\, L}$
Closed Geometry	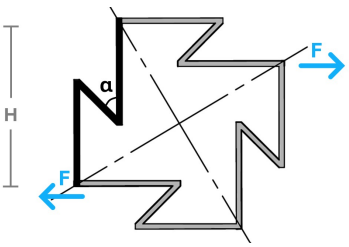	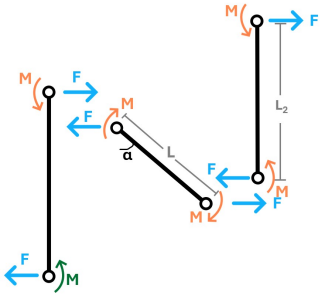	$H = 2L_2 - \cos(\alpha)\, L$ $3M = F\, H$ $F = \frac{3M}{2L_2 - \cos(\alpha)\, L}$

Table 1: Free body diagrams, where the moments shown in green are counteracted upon tessellation, and the corresponding force–moment relations for the base families defined by Roberjot [4].

C Appendix C: Overview of Archimedean solids and uniform 3D tessellations

Grünbaum [26] presented a comprehensive classification of uniform tilings of three-dimensional Euclidean space. These tilings are constructed from uniform polyhedra, including infinite families of prisms and antiprisms, the five Platonic solids, and the thirteen Archimedean solids. Archimedean solids are characterised by faces that are regular polygons, with identical vertex configurations throughout the polyhedron. These polyhedra are illustrated in Figure 14.
In total, Grünbaum identified 28 uniform space-filling tilings composed of such polyhedra. A subset of these tilings can be interpreted as stacks of planar slab-like tessellations, denoted by *S1–S14*. Of these, eleven slabs are directly derived from the eleven uniform two-dimensional tilings through prism extrusion, while slabs *S12–S14* represent distinct, non-prismatic layer constructions.
The complete list of the 28 uniform tilings, together with their polyhedral compositions, slab classifications, and ratios of constituent solids, is reproduced below following Grünbaum's original notation.

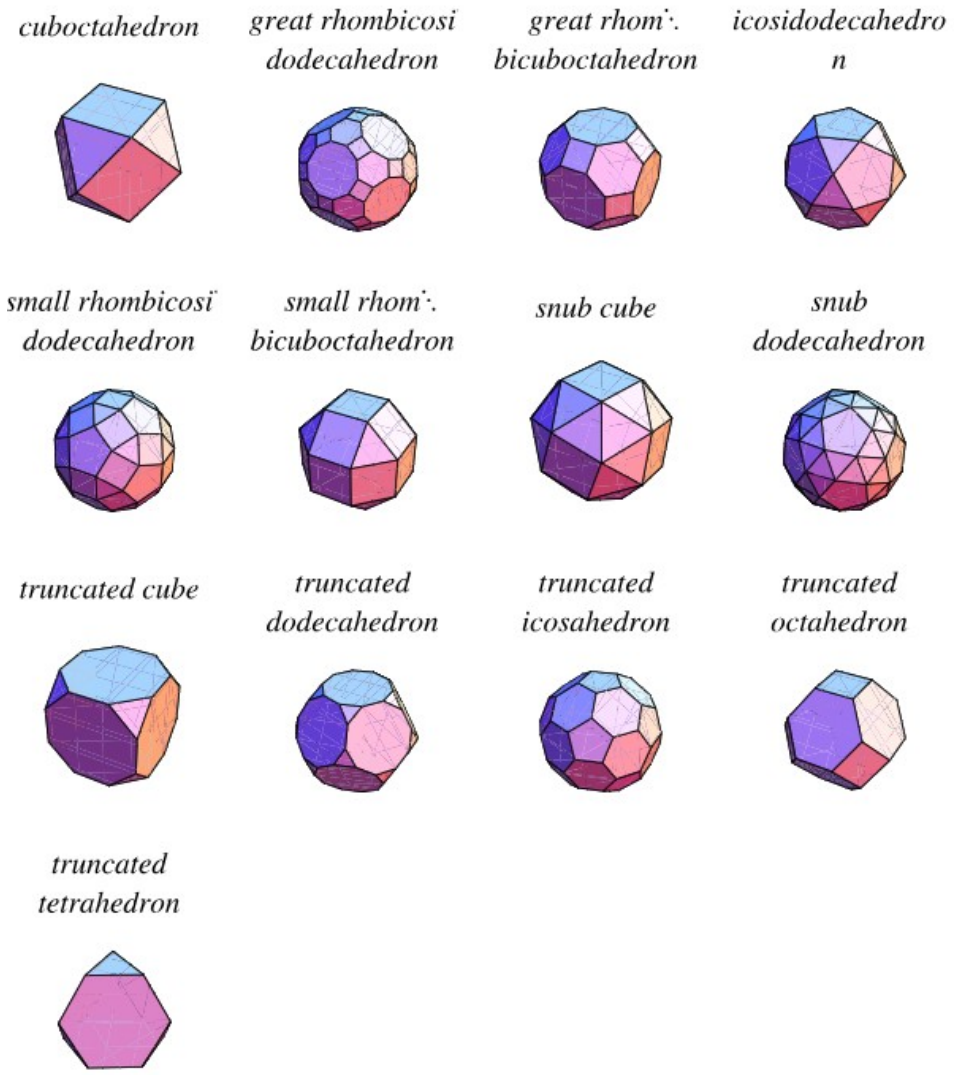

Figure 14: Overview of the Archimedean solids from Wolfram [27]

#1: ratio 1 : 2. Tetrahedra and octahedra; stacks of S12, with tetrahedra and octahedra meeting at boundaries of slabs.
#2: ratio 1 : 2. Reflected layers of octahedra and tetrahedra; stacks of S12, with tetrahedra meeting tetrahedra and octahedra meeting octahedra at boundaries of slabs.
#3: ratio 2 : 1 : 3. Alternating layers of 3-sided prisms and layers of tetrahedra and octahedra; slabs S12 (as in #1) intercalated by slabs of S1.

#4: ratio 2 : 1 : 3. Alternating layers of 3-sided prisms and reflected layers of octahedra and tetrahedra; slabs S12 (as in #2) intercalated by slabs of S1.
#5: ratio 2 : 1 : 1. Tetrahedra, rhombicuboctahedra and cubes.
#6: ratio 1 : 1. Tetrahedra and truncated tetrahedra; stacks of slabs S13.
#7: ratio 1 : 1. Octahedra and cuboctahedra.
#8: ration 1 : 1. Octahedra and truncated cubes.
#9: ratio 1 : 1 : 3. Cuboctahedra, rhombicuboctahedra and cubes.
#10: ratio 1 : 2 : 1. Cuboctahedra, truncated tetrahedra and truncated octahedra.
#11. Layers of three-sided prisms; stacks of S1.
#12. Square-faced layers of three-sided prisms, rotated 90°; stacks of slabs S14.
#13: ratio 2 : 1. Layers of prisms over (3.3.3.4.4); stacks of S2.
#14: ratio 2 : 1. Layers of prisms over (3.3.4.3.4); stacks of S3.
#15: ratio 2 : 1. Alternating layers of square-faced layers of three-sided prisms and cubes; the layers of prisms related by rotations; slabs S14 (as in #12) intercalated by slabs of S8.
#16: ratio 2 : 3 : 1. Layers of prisms over (3.4.6.4); stacks of S4.
#17: ratio 8 : 1. Layers of prisms over (3.3.3.3.6); stacks of S5.
#18: ratio 2 : 1. Layers of prisms over (3.6.3.6); stacks of S6.
#19: ratio 2 : 1. Layers of prisms over (3.12.12); stacks of S7.
#20: ratio 1 : 1 : 3 : 3. Rhombicuboctahedra, truncated cubes, cubes and octagonal prisms.
#21: ratio 2 : 1 : 1. Truncated tetrahedra, truncated cubes and truncated cuboctahedra.
#22: Cubes; stacks of S8.
#23: ratio 3 : 2 : 1. Layers of prisms over (4.6.12); stacks of S9.
#24: ratio 1 : 1. Layers of prisms over (4.8.8); stacks of S10.
#25: ratio 3 : 1 : 1. Cubes, truncated octahedra and truncated cuboctahedra.
#26. Layers of hexagonal prisms; stacks of S11.
#27: ratio 3 : 1. Octagonal prisms and truncated cuboctahedra.
#28: Truncated octahedra.

D Appendix D: Conceptual Extension to Archimedean Solid Honeycombs

This appendix presents an exploratory unit cell design to illustrate a potential direction for future research.. This unit cell is based on a great rhombicuboctahedron honeycomb (see Figure 14) and employs spatial, rather than planar, bases. Each base connects to adjacent bases at the vertices of a conceptual inner great rhombicuboctahedron. The bases themselves are based on the Connected Stars (CS) topology and incorporate a number of in-plane copy rotations equal to the number of vertices of the corresponding face. The outer honeycomb, defined by the great rhombicuboctahedron, provides attachment points at the centre of each face. Initial sketches of this conceptual structure are shown below. These sketches do not represent a complete unit cell, but rather provide a partial and illustrative visualisation of the proposed geometric concept. In the illustrations, red denotes octagonal faces, blue denotes hexagonal faces, and grey denotes square faces. The drawings are intended purely to convey the underlying geometric idea and the potential of combining spatial bases with Archimedean solid honeycombs, rather than to depict a finalised or optimised design.

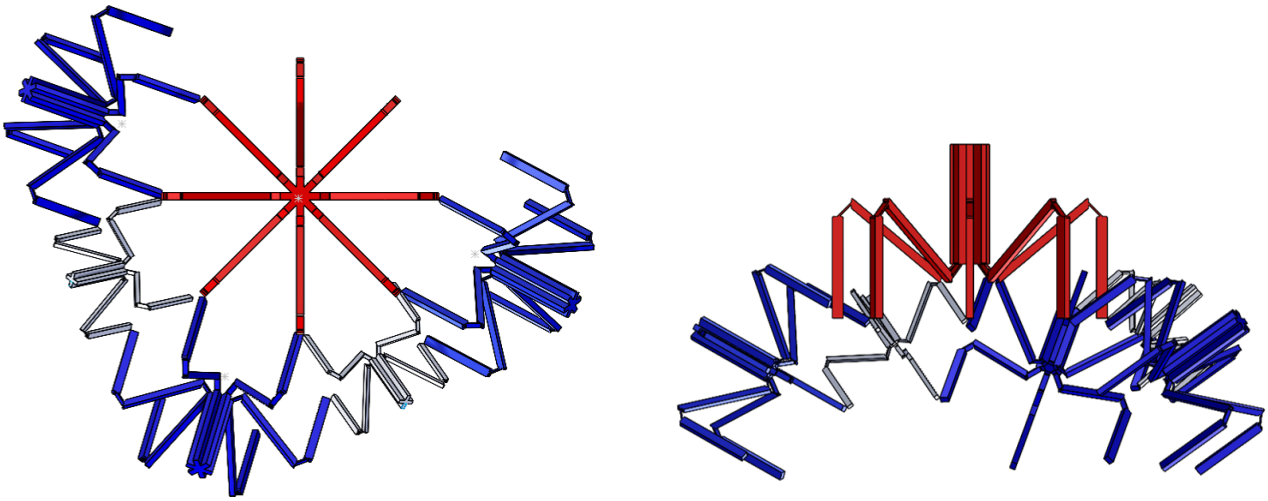

Figure 15: Upper and side views of a conceptual great rhombicuboctahedron-based unit cell, showing the proposed spatial base arrangement.

E Appendix E: An improved analytical model

In the initial analytical model, the characteristic length L was defined as

$$L = \frac{H}{sin(\alpha_0)}.$$

This definition implicitly includes the flexural segments as well as half of the beam height at both the top and bottom of the printed connected-star base. In the refined analytical model, the beam length is instead defined as the length of the inclined beam segment present in the printed geometry. As a consequence, the difference between the two definitions is represented by two vertical segments of length $l = 4.42mm$ each, which together account for the excluded beam height while preserving the overall structural height.
A schematic representation of the improved analytical model is shown in Figure 16. The corresponding z-displacement results, including those of the revised analytical model, are compared with the numerical and experimental results in Figure 17.

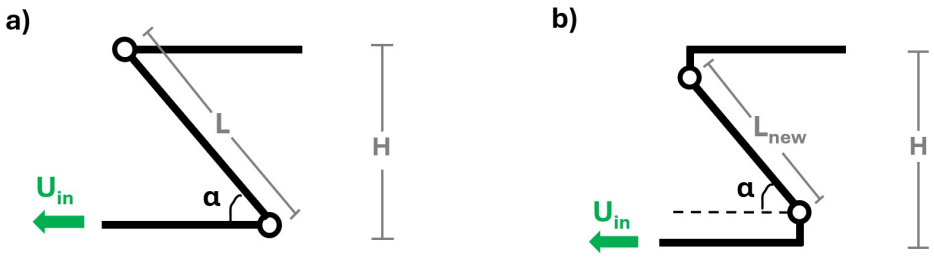

Figure 16: Improved analytical model

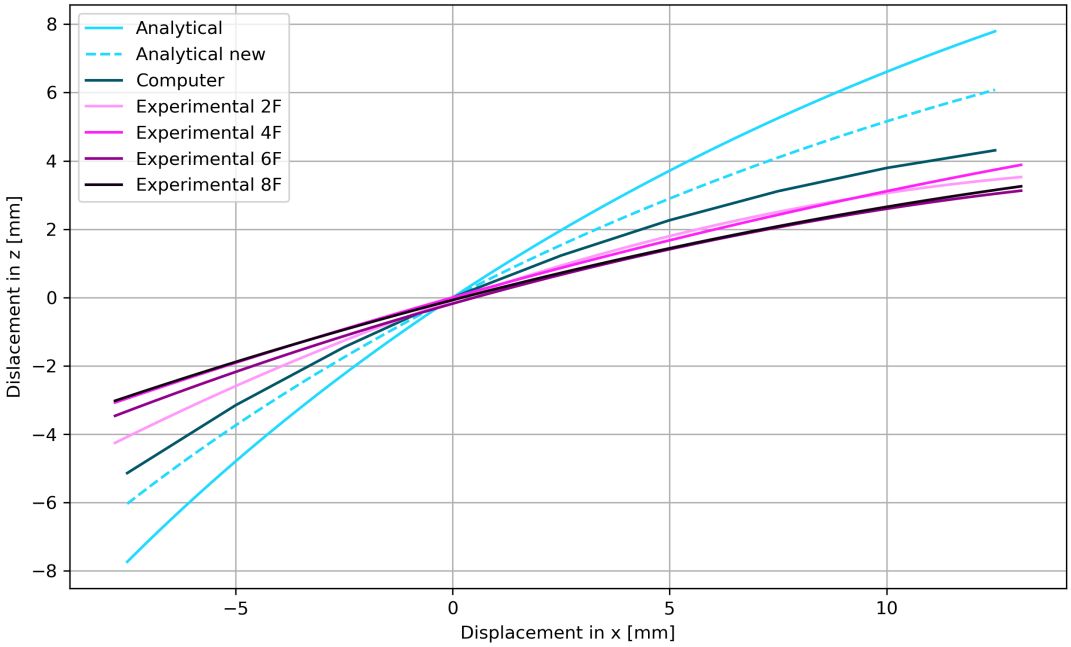

Figure 17: An overview of the z displacement of each model, including the new analytical model